AD-A037 142   NORTHROP CORP ANAHEIM CALIF ELECTRO-MECHANICAL DIV   F/G 17/5
              EXPERIMENTAL DEVELOPMENT OF A FLIR SENSOR PROCESSOR.(U)
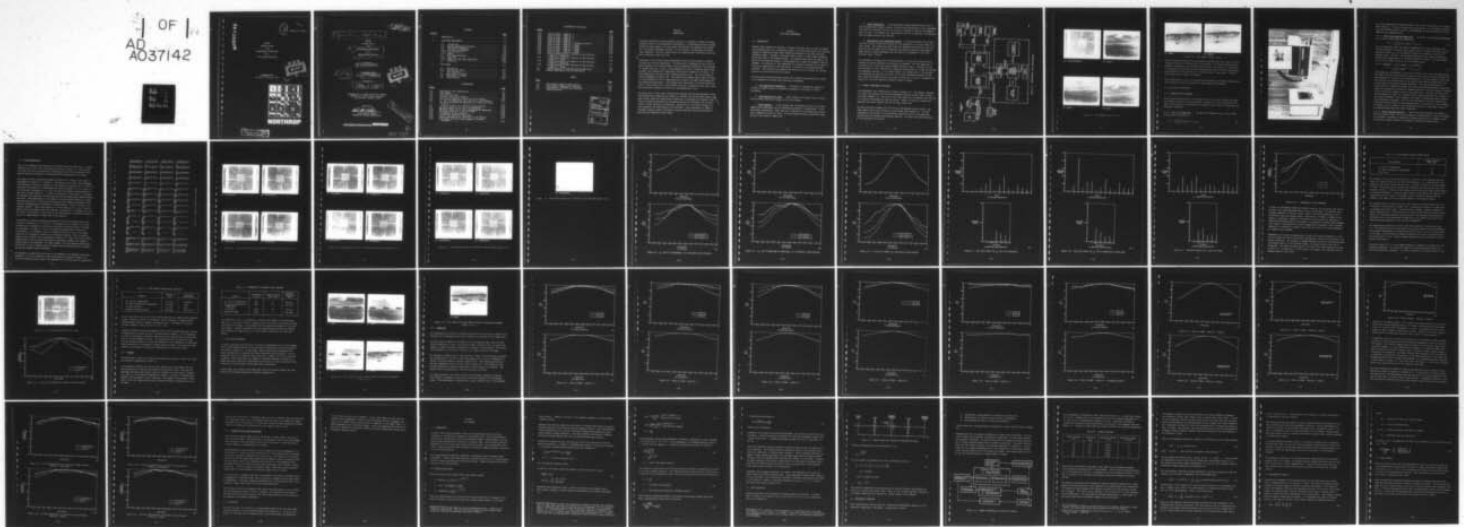   FEB 77   T NODA, H HENNING, T LEIBOFF, B DEAL   DAAG53-76-C-0188
UNCLASSIFIED   NORT-77Y016A   NL
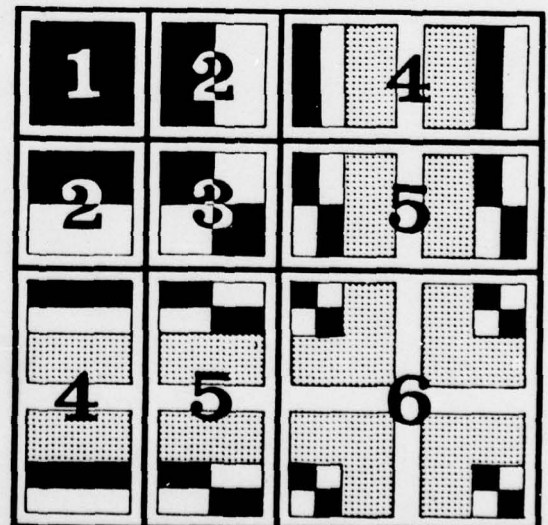
1 OF 1
AD
A037142

END
DATE
FILMED
4-77

ADA037142

SECOND
QUARTER REPORT
FOR
EXPERIMENTAL DEVELOPMENT
OF A
FLIR SENSOR PROCESSOR

D D C
MAR 18 1977
C

31 January 1977
(Revised 17 February 1977)

NORTHROP

(9) Quarterly rept. no. 2,

SECOND

QUARTER REPORT

FOR

(6) EXPERIMENTAL DEVELOPMENT

OF A

FLIR SENSOR PROCESSOR.

Contract
(15) DAAG53-76-C-0188

(12) 54 p.

31 January 1977

(Revised 17 February 1977)
(11)

Prepared by

(10) T./Noda,   T./Leiboff
      H./Henning,   B./Deal

Prepared for U.S. Army Electronics Command,
DRSEL-NV-V1, Night Vision Laboratory,
Fort Belvoir, Virginia, 22060

Approved by

Ross M. Chiles

Ross Chiles, Manager
Automation Systems Engineering

388 834

CONTENTS

ILLUSTRATIONS

ILLUSTRATIONS (Continued)

SECTION I
INTRODUCTION

Northrop Corporation, Electro-Mechanical Division, is pleased to submit the second quarterly report on the Experimental Development of a FLIR Sensor Processor program. During the first quarter, the test system configuration was assembled and checked out, the software debugged, and Task I of the contract, the Experiment and Study Plan, completed. The first quarter report was submitted and a technical review was held at Northrop October 18, 1976.

This report, which covers the work performed during the second quarter, primarily concerns the autofocus experiments. The object was to determine the use of the 2D Haar processor as an accurate sensor of in-focus/defocus conditions in FLIR systems. To validate this use, a series of measurements were taken to determine sensitivity, accuracy, and repeatability (temporarily substituting a camera for the FLIR). Initial measurements were made using a RETMA resolution chart. This was followed by using thermograms provided by NVL. The analysis and graphed results show the effect of focus adjustment on the ac magnitudes and ac power of the Haar coefficients and the generalized descriptors. Using imagery with some amount of activity within the view, it can be shown that a simple scalar value can be computed in real time, which has a sensitivity greater than the eye in determining best focus.

The second part of this report discusses the automatic deblurring experiments, which have already been started and are planned to continue into the following quarter. They involve analog and computational simulations, an experimental evaluation technique, alternative approaches for estimating unknown blur functions, and the application of these functions to deblurring. Application of the 2D Haar processor to blur estimation and deblurring is fully discussed. Other experiments in image enhancement, adaptive signal processing, and data compression have been started but have not been described in this report.

SECTION 2
AUTO FOCUS EXPERIMENTS

2.1 INTRODUCTION

Because severe demands are placed on a two-man helicopter team, the need for manual FLIR refocusing can pose a formidable problem. FLIR defocusing arises from continual changes in observation range, small thermal deformations of the lens, and other incidental causes. Automatic refocusing offers a means to combat these tendencies and relieve part of the manpower burden. The apparatus must sense the defocus condition of the image and produce a corresponding error signal for automatic lens adjustment. The objective of this experiment is to develop a measure of the state of focus of an image based on the distribution of energy in its rationalized Haar transform. The resultant focus measure may then be used as the basis for the generation of a focus-correcting error signal.

The focus measure developed should exhibit the following characteristics in order to be compatible with system and operational requirements:

a. <u>Low Computational Complexity</u> - The amount of computation required to evaluate an image's state of focus must be amenable to real-time (TV rates) processing.

b. <u>High Sensitivity to Focus</u> - Small changes in an image's state of focus should produce significant changes in the focus measure.

c. <u>Noise Immunity</u> - In the present test configuration, noise in the video signal before digitization is the overriding contributor to system noise. In an operational configuration, small (one pel) translations of the image may also produce a significant amount of noise. The focus measure should be relatively insensitive to both types of image noise.

d. <u>Scene Independence</u> - The focus measure should perform equally well on both background and targets; however, there are some limitations to this requirement. There must be sufficient activity in the area of interest to evaluate the image's state of focus. For example, any focus measure will not be expected to perform well when the image contains only clear sky.

e. <u>Adaptability in an Operational System</u> - The focus measure in its final form must be able to serve as the basis for the generation of an error signal in a servo system. This signal must have sufficient bandwidth and stability to be compatible with FLIR image quality parameters and ASH/AAH operational requirements. These specific system requirements are discussed in the Appendix to the first quarterly report (76Y133).

The experiment is divided into two major sections. In the first section the performance of several candidate focus measures is examined. The test image used in this section is a video test pattern (RETMA resolution chart). Tradeoffs of the characteristics of the candidate focus measures are made and two of them are selected for subsequent analysis. In the second section, the capabilities of the selected focus measures are evaluated on the set of five FLIR thermograms supplied by NVL. Both target and background objects are used as input data in order to determine the behavior of the focus measures on general classes of images.

2.2 GENERAL EXPERIMENTAL PROCEDURE

The experimental test configuration is shown in Figure 2-1. Test imagery consisted of a video test pattern and five FLIR thermograms supplied by Night Vision Laboratory (NVL) (Figure 2-2). The focus of the video camera was set manually with the aid of 13 equally spaced marks on the lens barrel. Figure 2-3 shows the optical rail apparatus and a more detailed view of the video camera lens.

The data collection sequence for each of the focus measures was as follows: The video camera lens was set initially at one extreme (lens position A). The Haar transforms of both fields of four previously selected sectors of the image were acquired and the candidate focus measure computed. The result was then printed out on the Centronics Line Printer.
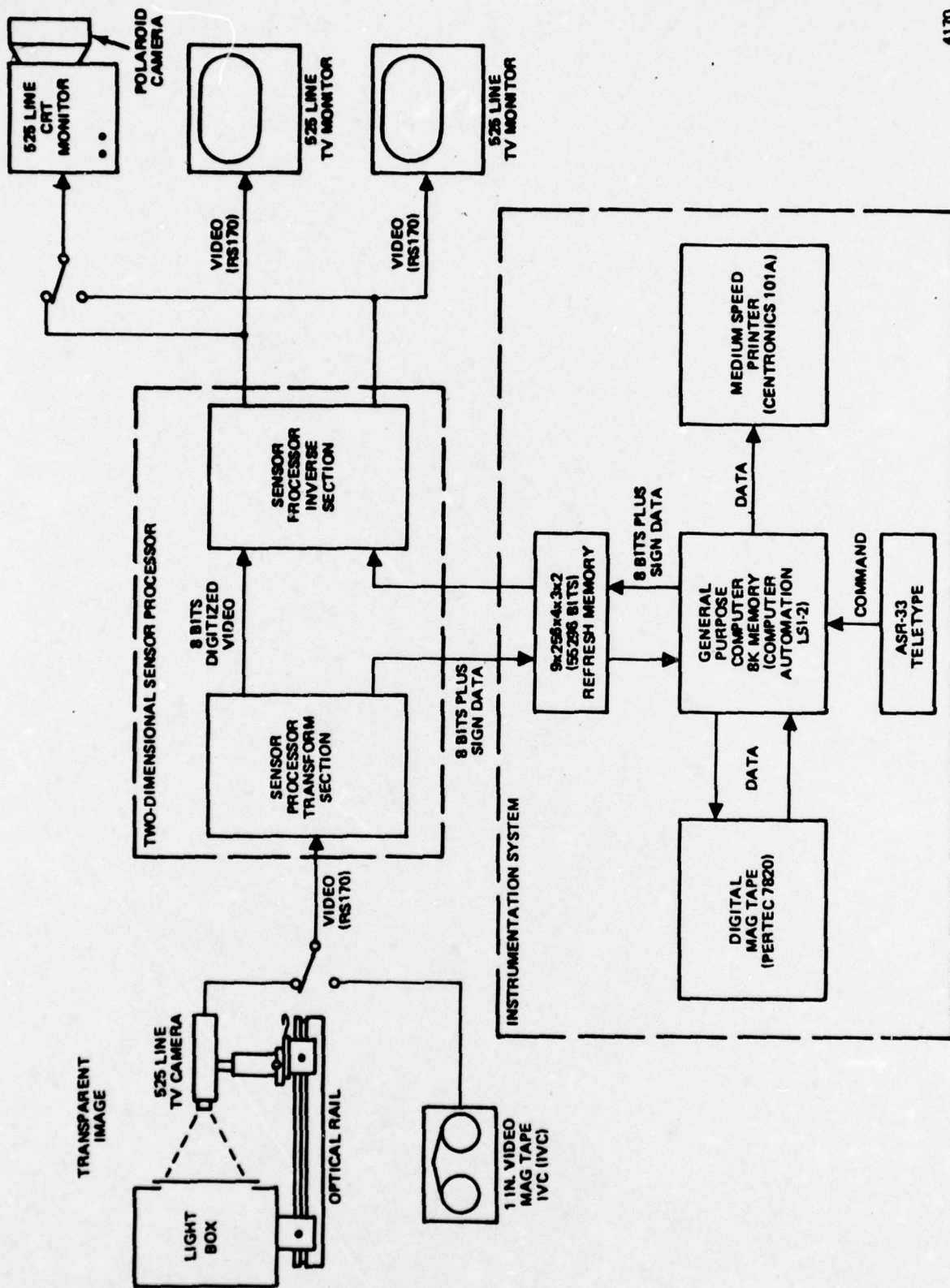
Figure 2-1. EXPERIMENTAL TEST CONFIGURATION

4170

2-3
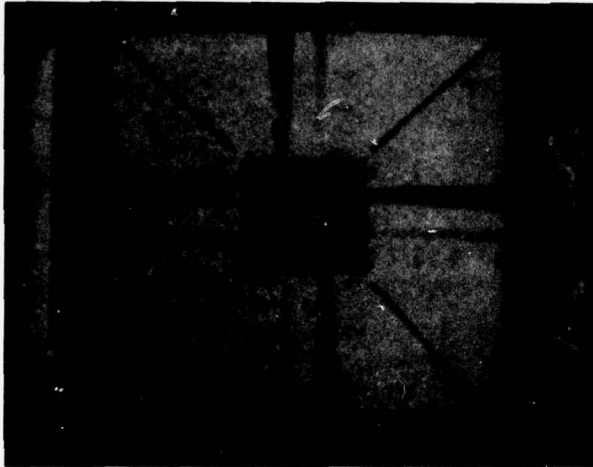
(A)　VIDEO TEST PATTERN
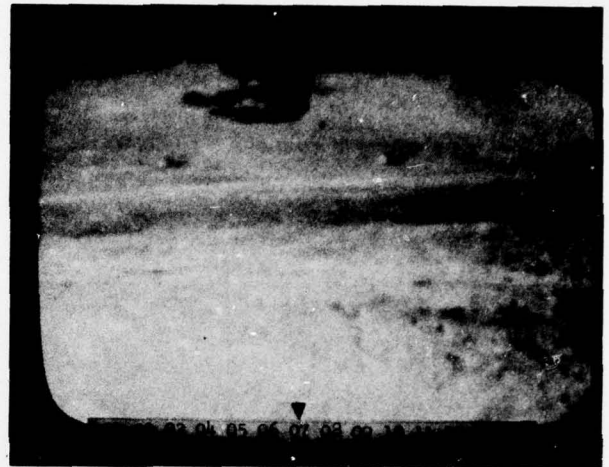
(B)　IMAGE 1
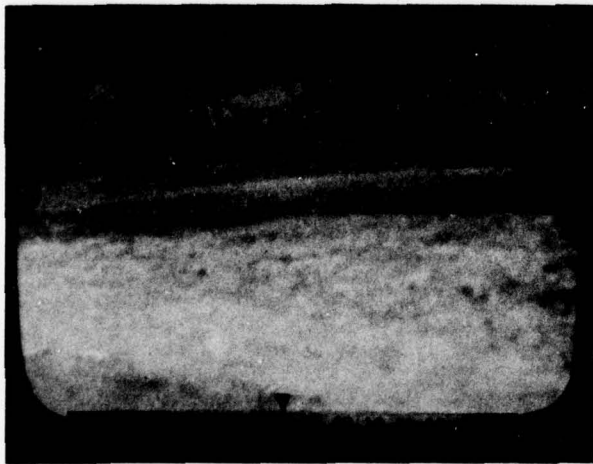
(C)　IMAGE 2
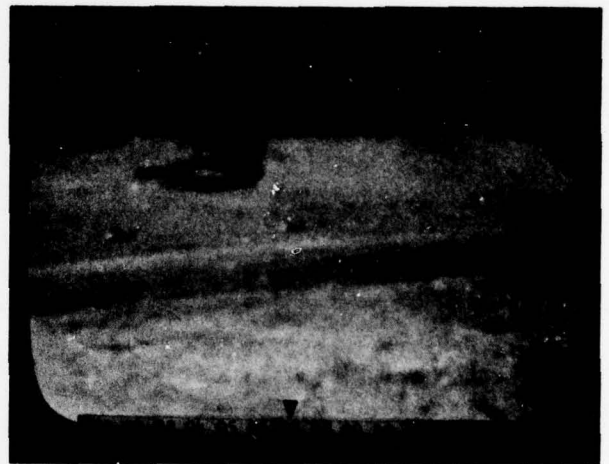
(D)　IMAGE 3

Figure 2-2.　TEST IMAGERY (Sheet 1 of 2)
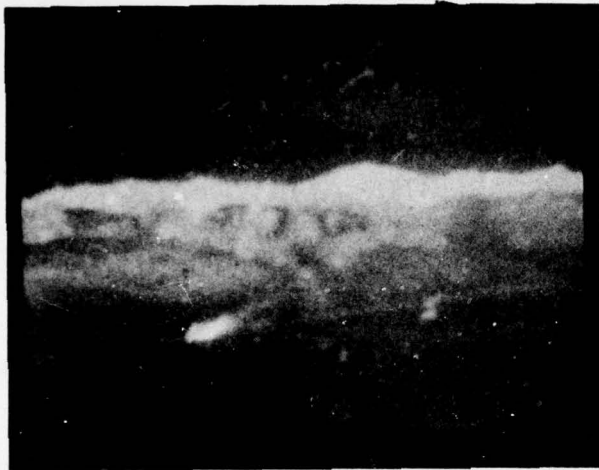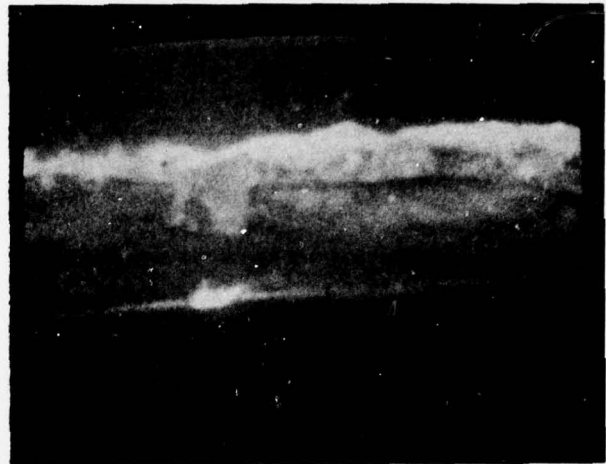
(E)   IMAGE 4   (F)   IMAGE 5

Figure 2-2.   TEST IMAGERY (Sheet 2 of 2)

This was repeated, advancing the lens position one step each time, until the other
extreme lens position (lens position M) was reached. The entire process was then
repeated, stepping the lens backward from position M to position A. This process
of advancing and retracting the lens position through one cycle while evaluating a
focus measure at each position will be referred to as a "Lens Cycle." One lens
cycle takes about 6 minutes to complete.

Noise measurements of each focus measure were performed by constantly computing the
focus measure's value while leaving the video camera lens stationary.

2.3   TEST PATTERN EXPERIMENT

2.3.1   Candidate Focus Measures

Several preliminary measures of an image's state of focus were selected for study.
Each measure is based on the distribution of energy in the Haar transform of the
image. The candidate focus measures are presented here in order of increasing com-
putational complexity.

2.3.1.1 Sum of the Magnitudes - The sum of the magnitudes, S_m, of the ac Haar
coefficients is expressed as

$$S_m = \sum_r \sum_m \sum_p \sum_n |a_{rmpn}| - a_{-1,1,-1,1} \tag{1}$$

Figure 2-3. AUTOFOCUS TEST SETUP

S_m is the computationally simplest index of the total ac information in an image's Haar transform. In order to ascertain the distribution of ac information throughout the transform as well, totals of the magnitudes of the coefficients were also taken for each sequency group.

2.3.1.2 Sum of the Normalized Magnitudes - The sum of the normalized magnitudes, S_n, of the ac coefficients is expressed as

$$S_n = \sum_r \sum_m \sum_p \sum_n f_{rp} |a_{rmpn}| - a_{-1,1,-1,1} \tag{2}$$

The two dimensional sensor processor's implementation of the rationalized Haar transform contains an inherent high sequency boost. To remove this boost, a normalization factor, f_{rp}, is introduced to weight the information from the rp^{th} sequency group. The sum of the normalized magnitudes more closely approximates the sum of the magnitudes of an unrationalized Haar transform. S_m was evaluated for all the ac terms as well as for each sequency group.

2.3.1.3 AC Power - The ac power, C, is defined as

$$C = \sum_r \sum_m \sum_p \sum_n (a_{rmpn})^2 - (a_{-1,1,-1,1})^2 \tag{3}$$

The parameter C is equivalent to the local activity of a 16 by 16 pel image sector. The image's activity should provide an index of focus that is more noise immune and more sensitive to focus than the previous measures. The noise immunity arises from the fact that, by squaring terms, a few large fluctuations in amplitude may still be seen despite the presence of many small ones. The increased sensitivity to focus is due to a similarity between the Fourier and unrationalized Haar transforms. Since both transforms are unitary and possess equivalent dc terms, Parseval's theorem tells us that the ac energy in each is also equivalent. Defocusing an image effectively subjects the image to a low-pass filter, thereby decreasing the ac energy in its Fourier transform. The ac energy in the image's unrationalized Haar transform would likewise be decreased. Since the rationalization of the Haar transform involves only simple scaling of each sequency group, the direction, if not the amount, of change in the ac energy of the rationalized Haar will be equivalent to that of the unrationalized Haar and Fourier transforms.

2.3.1.4 Texture and Edge Activity - Texture and edge activities, as defined in the first quarter report, are the most expensive computationally. They are included in the study to determine if variations in image activity due to changes in state of focus will appear primarily as variations in texture or edge activity.

2.3.2 Focus Measure Data

Each of the foregoing focus measures was computed through one lens cycle. A representative portion of a lens cycle printout is shown in Figure 2-4. Since during each lens cycle each lens position is encountered twice, the two resultant focus measure values are averaged to facilitate graphical presentation of the data.

The range of defocus encountered through one lens cycle is shown in the series of photographs in Figure 2-5, A through M. The behavior of the first three candidate focus measures is shown as a function of lens position in Figures 2-6, 2-7, and 2-8. The noise characteristics of each measure are shown in Figures 2-9, 2-10, and 2-11. As can be seen in Figures 2-6, 2-7, and 2-8, each focus measure tested exhibited a peak value at lens position G. In order to determine if lens position G is indeed the sharpest focus position, the fine detail of the test pattern was observed under a hand lens. Close examination of the wedges in the test pattern (Figure 2-5) shows that lens positions F, G, and H are the ones that yield images with sharper focus. Visually discriminating the difference in focus between F, G, and H is next to impossible, however. Since lens position G is in the center of F, G, and H, and the peaks in the focus measure curves are distinct, lens position G is deemed to be the "in focus" lens position. The ability of the focus measure to evaluate the state of focus of an image appears to rival that of the observer.

The division of energy into sequency groupings for each focus measure can be seen in part A of Figures 2-6, 2-7, and 2-8. The changes in the ac energy of the Haar transform due to movement of the lens are localized in sequency groups 11 through 15, and groups 7 through 10. Also, both sequency groupings tend to behave in a like fashion. It is possible, then, to evaluate the state of focus of an image using only the information contained in one sequency grouping. Such an approach, however, would increase the focus measure's sensitivity to image noise (particularly image motion) as well as allow some possibly significant changes in ac energy in another group to go unobserved. For these reasons, the focus measures studied here will sum all of the ac energy within the image's Haar transform and will not single out any one sequency group or grouping.

The sharpness, or sensitivity to focus, of the candidate focus measures varies substantially. To aid in comparison, each focus measure is plotted in Figure 2-12. The curve resulting from the sum of the magnitudes of ac coefficients is comparative-

LENS POSITION A

SECTOR	GRP1	GRP2	GRP3	GRP4	GRP5	GRP6	GRP7	GRP8	GRP9	GRP10	GRP11	GRP12	GRP13	GRP14	GRP15	AC
	AUTO FOCUS		GROUP POWER													
2290	325	82		19		1	14	7	6	16	25	5	23	96	116	410
229E	325	82		31		2	22	7	8	8	39	7	26	70	147	449
2300	329	65	1		1	2	13	2	7	7	9	5	16	42	85	259
230E	330	64	1	15		2	23	3	10	11	19	5	21	56	136	367
2310	327	29	1	6	3	2	7	3	7	14	4	4	14	66	107	267
231E	327	29	1	3	2	3	6	6	5	7	5	5	18	81	132	303
2320	320	5		6	2			3	5	10	4	4	19	45	68	172
232E	320	5		5	1	2	1	3	10	7	5	9	16	54	84	202
	325	45		11	1	1	10	4	7	10	13	5	19	63	109	303

LENS POSITION B

SECTOR	GRP1	GRP2	GRP3	GRP4	GRP5	GRP6	GRP7	GRP8	GRP9	GRP10	GRP11	GRP12	GRP13	GRP14	GRP15	AC
	AUTO FOCUS		GROUP POWER													
2290	325	82		12		2	16	5	16	16	14	7	27	80	98	376
229E	325	82		36		3	29	4	10	18	28	8	20	86	97	421
2300	329	65				3	7	3	11	7	12	4	15	47	65	247
230E	329	50	1	10	1	6	23	4	14	8	32	7	13	65	76	310
2310	326	20	1	11	3	6	5	5	10	13	3	4	18	84	126	309
231E	327	29	1	6	3	2	7	2	12	7	6	3	9	75	129	291
2320	320	5		5	1	1	3	2	4	7	5	5	18	41	94	190
232E	320	5		2		2	3	3	6	14	2	7	22	59	112	240
	325	42		11	1	3	11	3	10	11	12	5	17	67	99	298

LENS POSITION C

SECTOR	GRP1	GRP2	GRP3	GRP4	GRP5	GRP6	GRP7	GRP8	GRP9	GRP10	GRP11	GRP12	GRP13	GRP14	GRP15	AC
	AUTO FOCUS		GROUP POWER													
2290	325	101		12		2	13	3	16	9	28	15	26	62	147	435
229E	325	92		39		2	20	8	9	11	27	5	22	81	117	425
2300	329	65			2	4	6	3	9	9	9	3	18	34	91	256
230E	329	50	1	9	1	6	16	4	11	10	31	5	24	48	76	293
2310	327	26	1	6	2	1	8	3	10	16	7	10	22	63	118	297
231E	327	26	1	6	6	3	11	4	7	13	9	9	14	54	146	308
2320	320	5		5	5	1	3	2	4	6	5	3	22	57	84	198
232E	320	2		2	2	1	3	2	3	6	6	4	13	78	71	193
	325	44		10	2	2	10	3	8	10	15	6	20	59	106	300

LENS POSITION D

SECTOR	GRP1	GRP2	GRP3	GRP4	GRP5	GRP6	GRP7	GRP8	GRP9	GRP10	GRP11	GRP12	GRP13	GRP14	GRP15	AC
	AUTO FOCUS		GROUP POWER													
2290	325	101		12		2	18	8	13	17	22	15	30	112	104	455
229E	325	82		22		2	21	3	13	13	32	10	26	59	122	406
2300	329	65		7	1	3	11	4	11	16	16	6	24	56	113	334
230E	329	50	1	14	3	6	21	2	16	20	11	5	29	73	102	353
2310	327	26	1	6	6	1	6	2	8	9	7	7	26	70	104	279
231E	327	26	1	3	4	1	10	4	9	16	4	6	16	92	118	310
2320	320	5		5	1	4	3	3	5	7	7	3	20	45	82	181
232E	320	5		9	2	2	3	3	6	11	9	5	20	46	93	212
	325	45			2	2	11	3	10	13	13	7	23	69	104	316

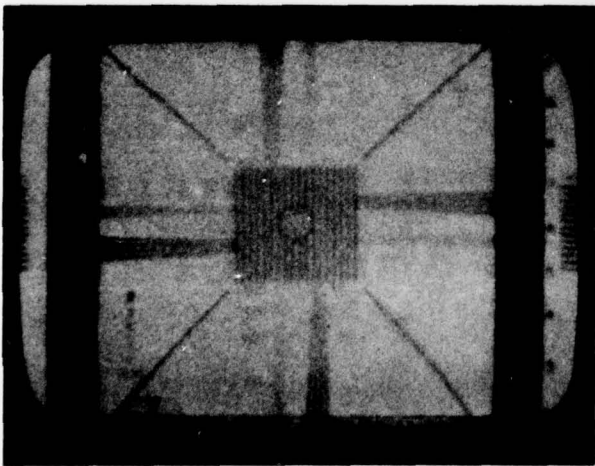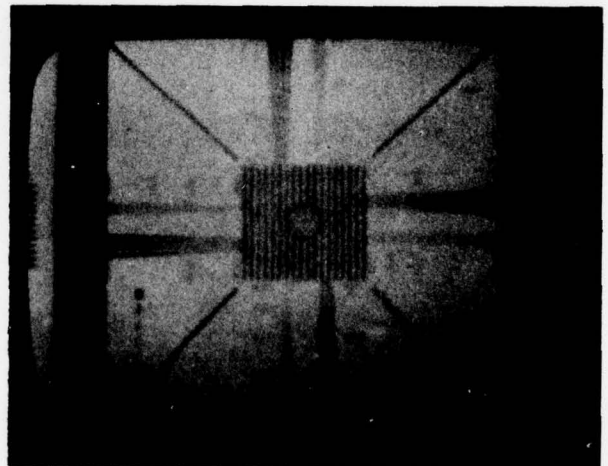Figure 2-4. PORTION OF LENS CYCLE PRINTOUT
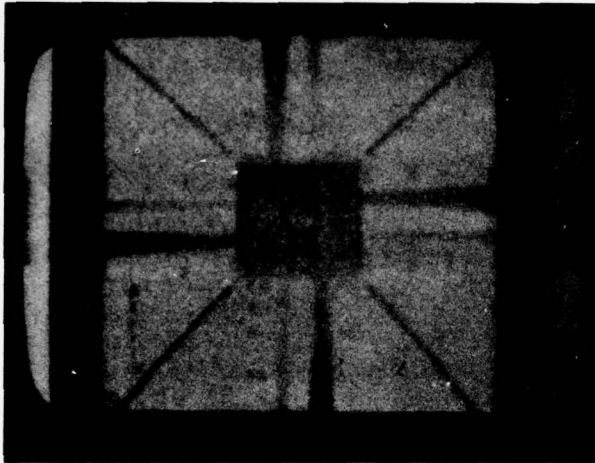
(A)   LENS POSITION A
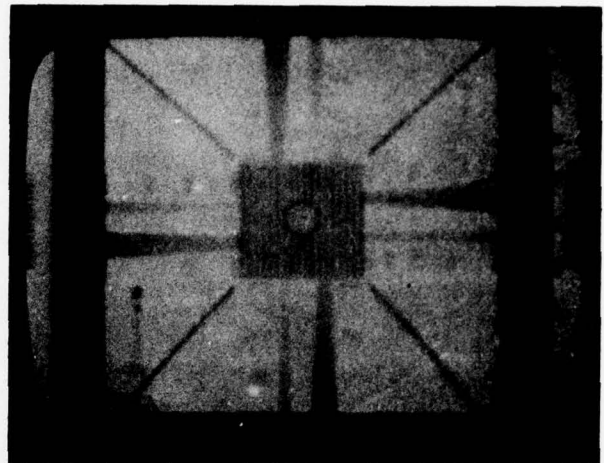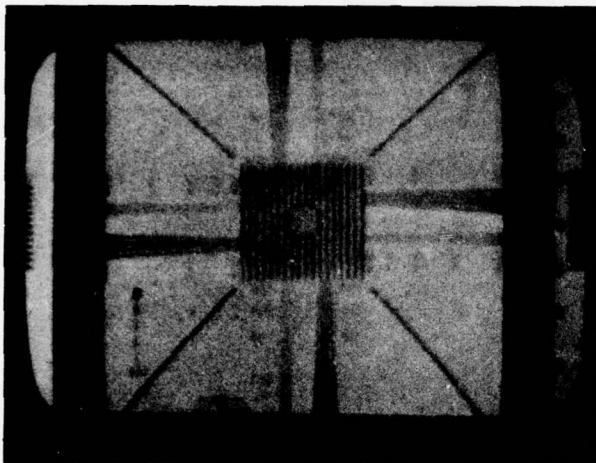
(B)   LENS POSITION B

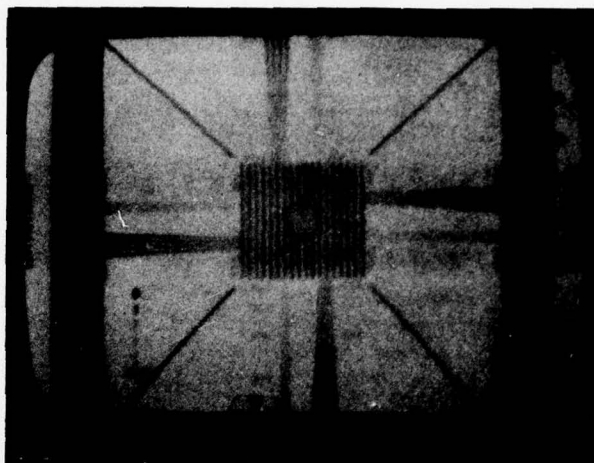(C)   LENS POSITION C

(D)   LENS POSITION D

Figure 2-5.   TEST PATTERN IMAGES AS A FUNCTION OF LENS POSITION (Sheet 1 of 4)
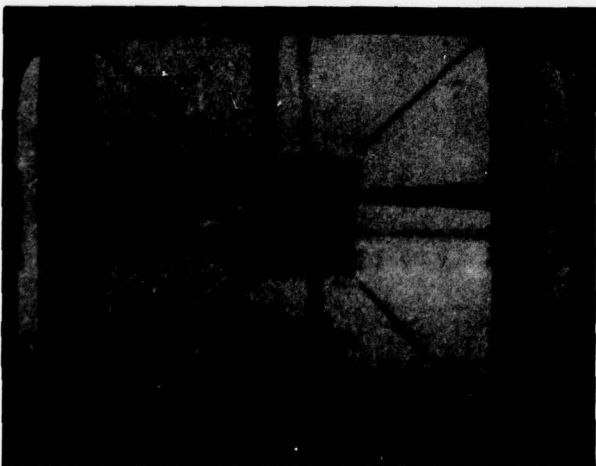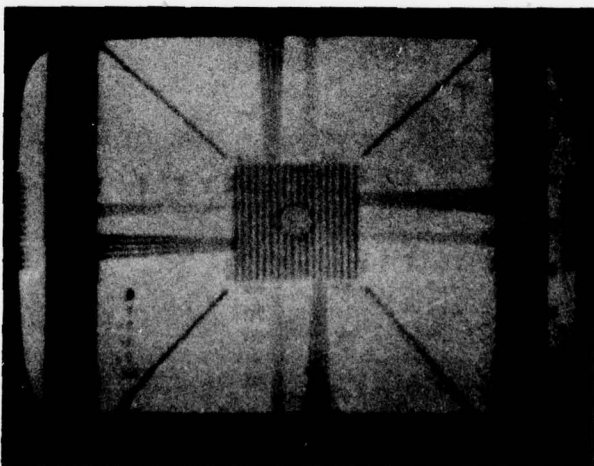
(E)   LENS POSITION E

(F)   LENS POSITION F

(G)   LENS POSITION G

(H)   LENS POSITION H

Figure 2-5.   TEST PATTERN IMAGES AS A FUNCTION OF LENS POSITION (Sheet 2 of 4)

(I) LENS POSITION I
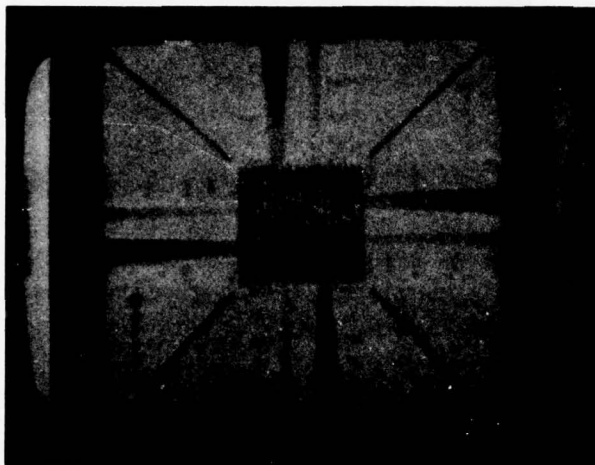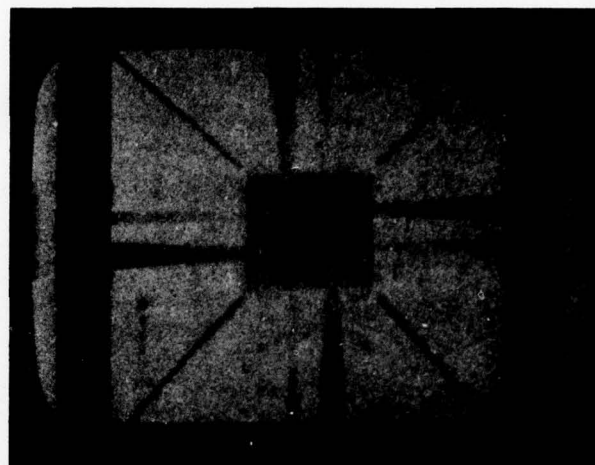
(J) LENS POSITION J
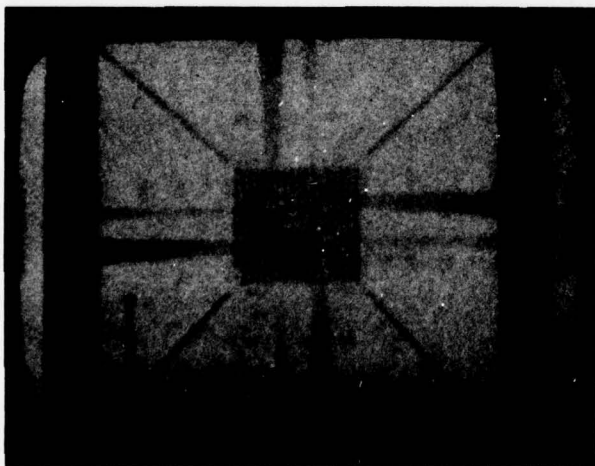
(K) LENS POSITION K
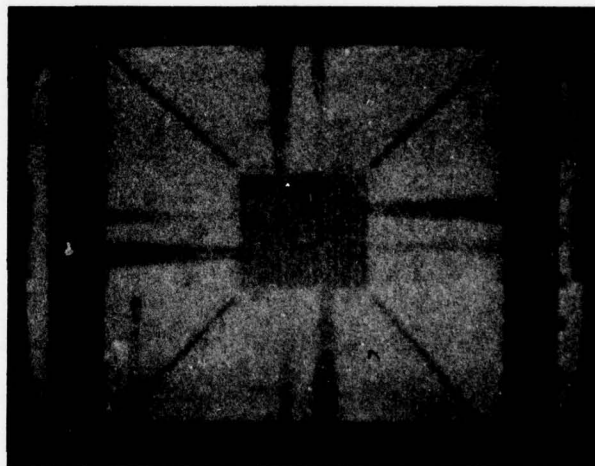
(L) LENS POSITION L

Figure 2-5. TEST PATTERN IMAGES AS A FUNCTION OF LENS POSITION (Sheet 3 of 4)

(M)　**LENS POSITION M**

Figure 2-5.　TEST PATTERN IMAGES AS A FUNCTION OF LENS POSITION (Sheet 4 of 4)
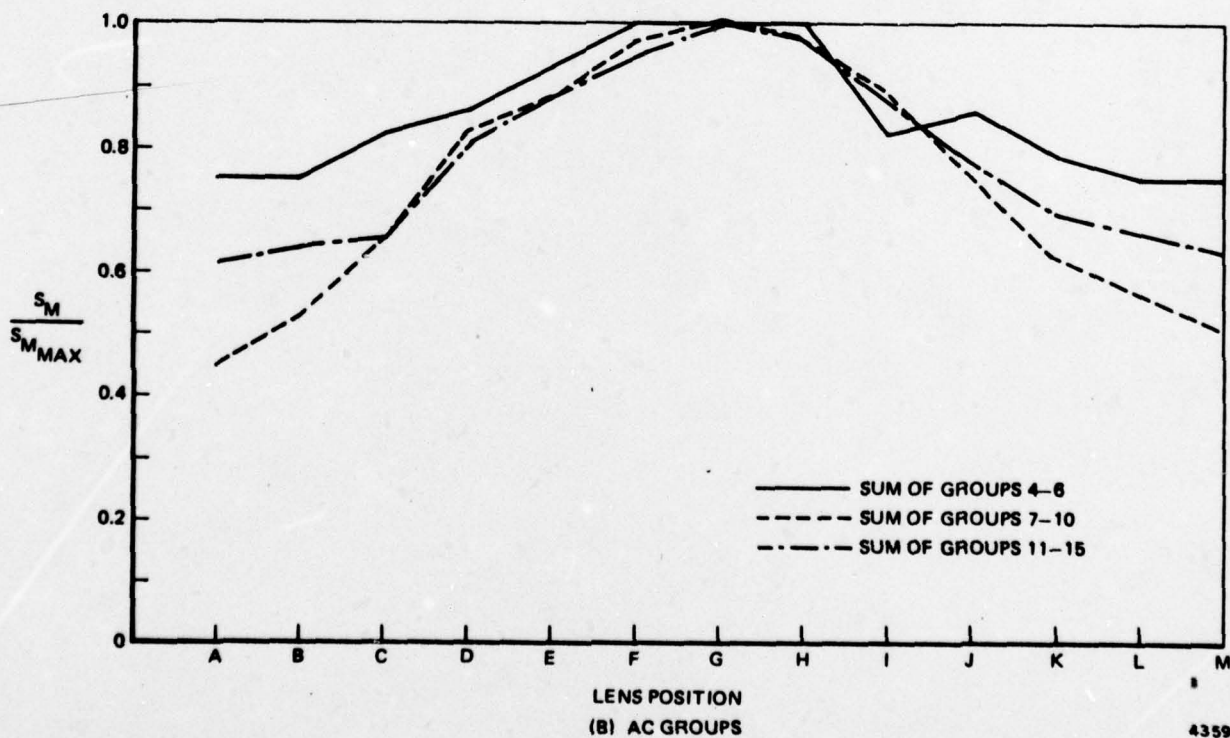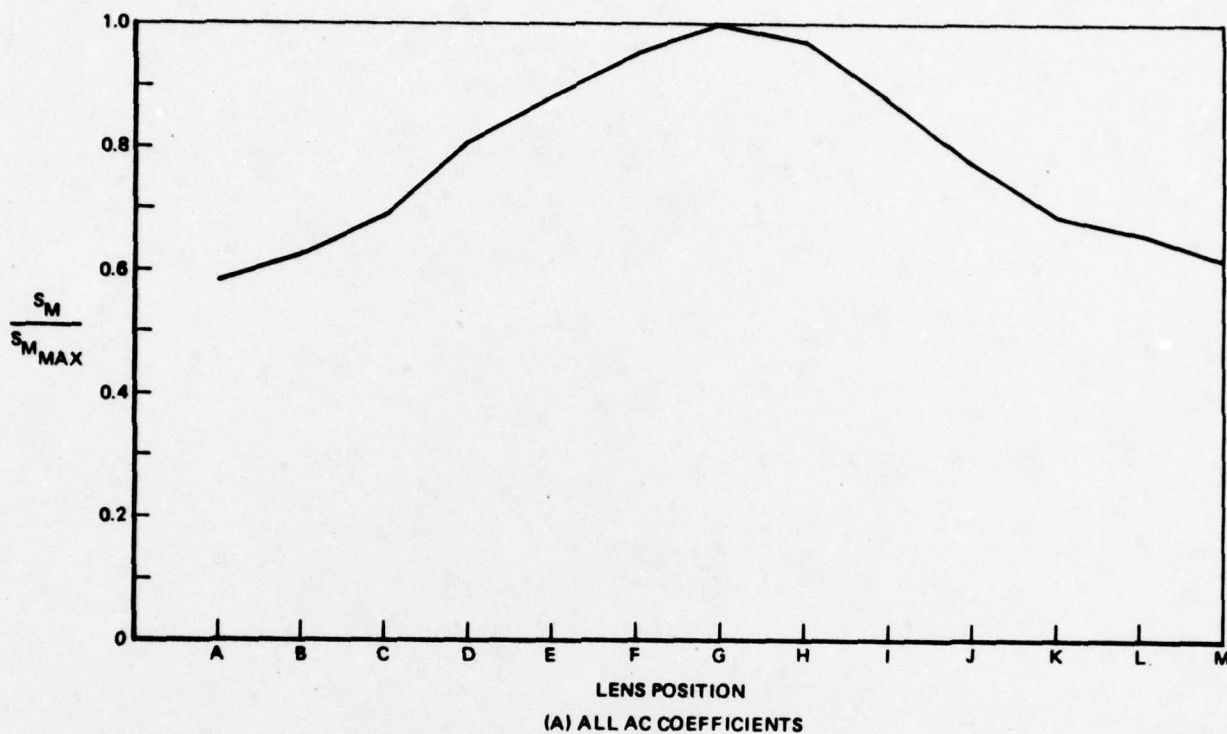
Figure 2-6. S_m, SUM OF AC MAGNITUDES, AS A FUNCTION OF LENS POSITION

2-14
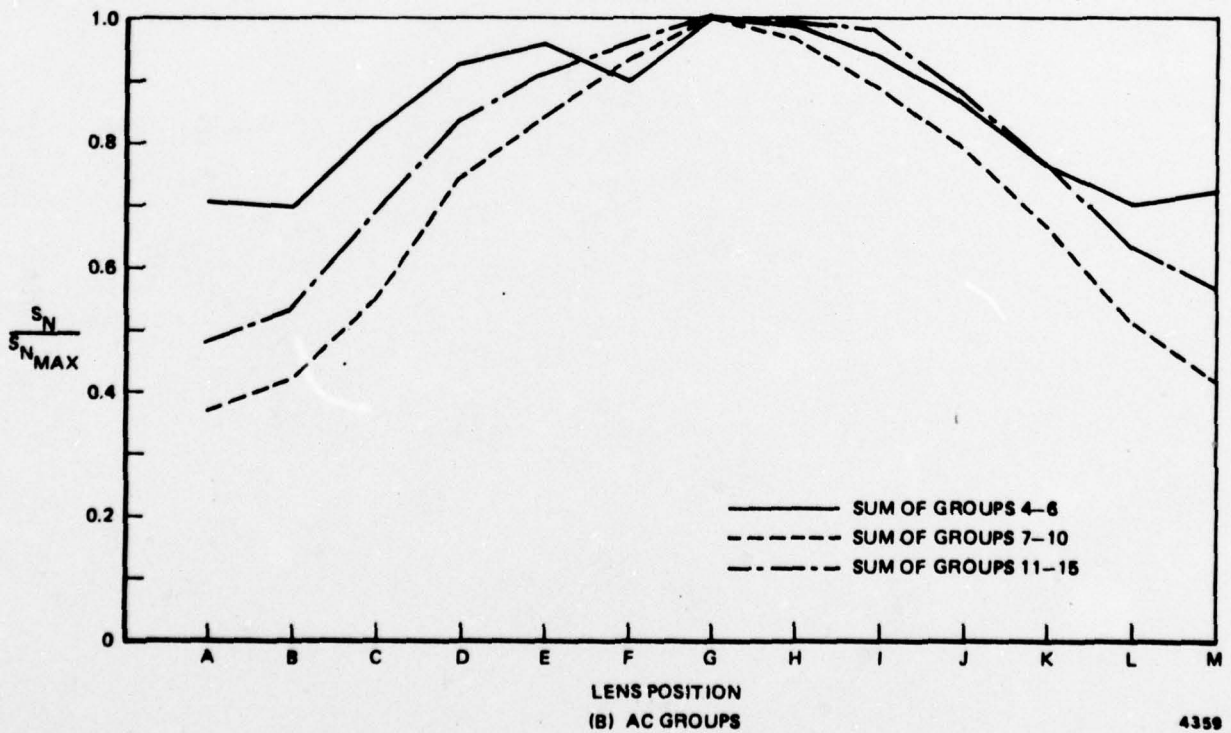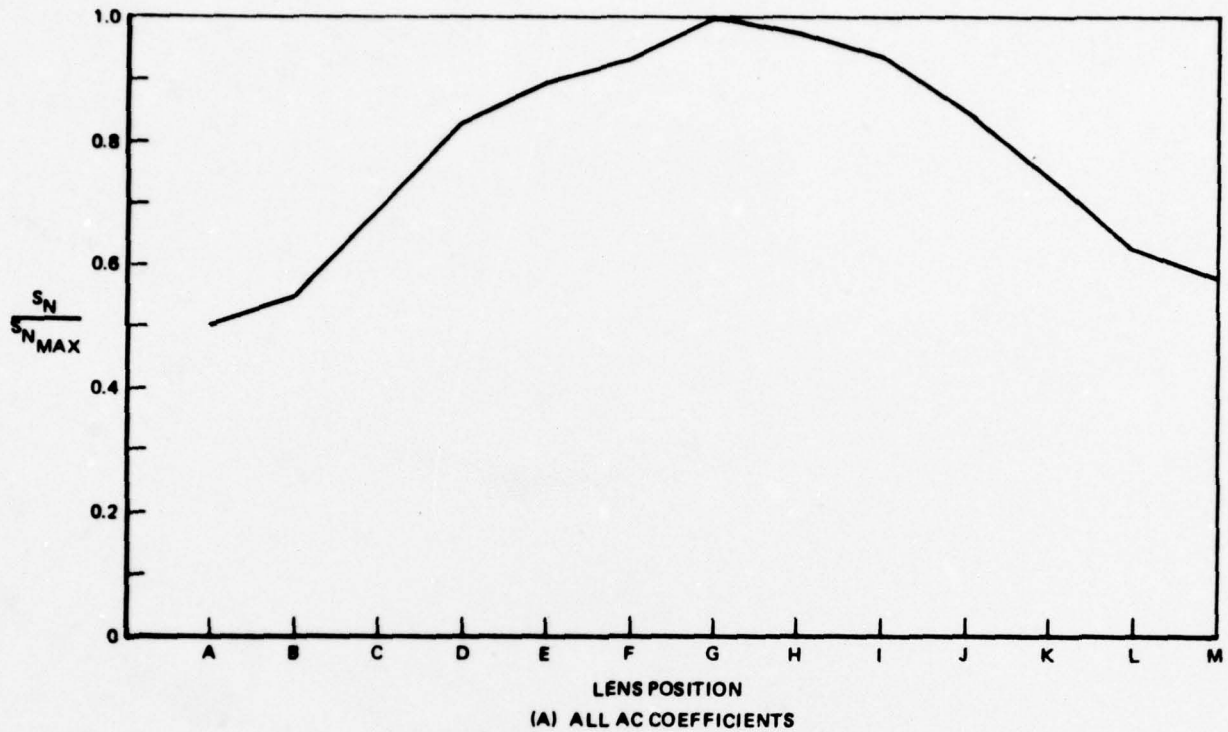
Figure 2-7. S_n, SUM OF NORMALIZED AC MAGNITUDES, AS A FUNCTION OF LENS POSITION

LENS POSITION

(A) ALL AC COEFFICIENTS

LENS POSITION

(B) AC GROUPS

SUM OF GROUPS 4–6
SUM OF GROUPS 7–10
SUM OF GROUPS 11–15
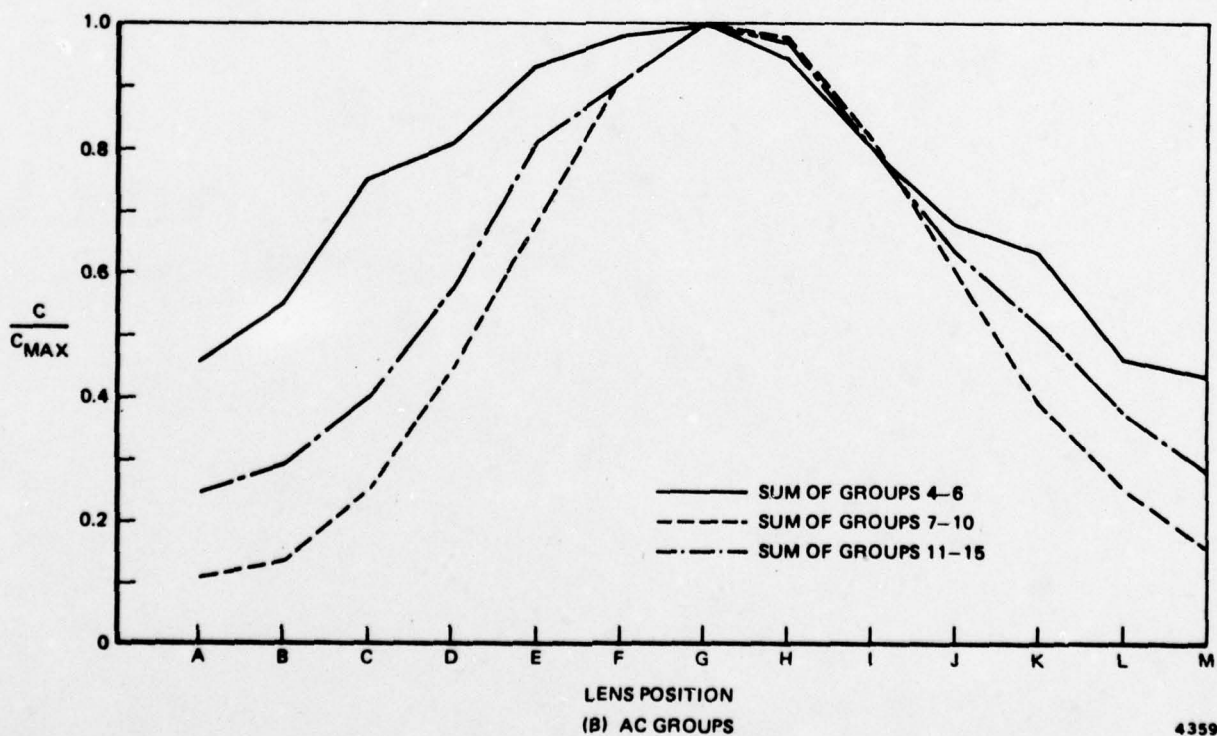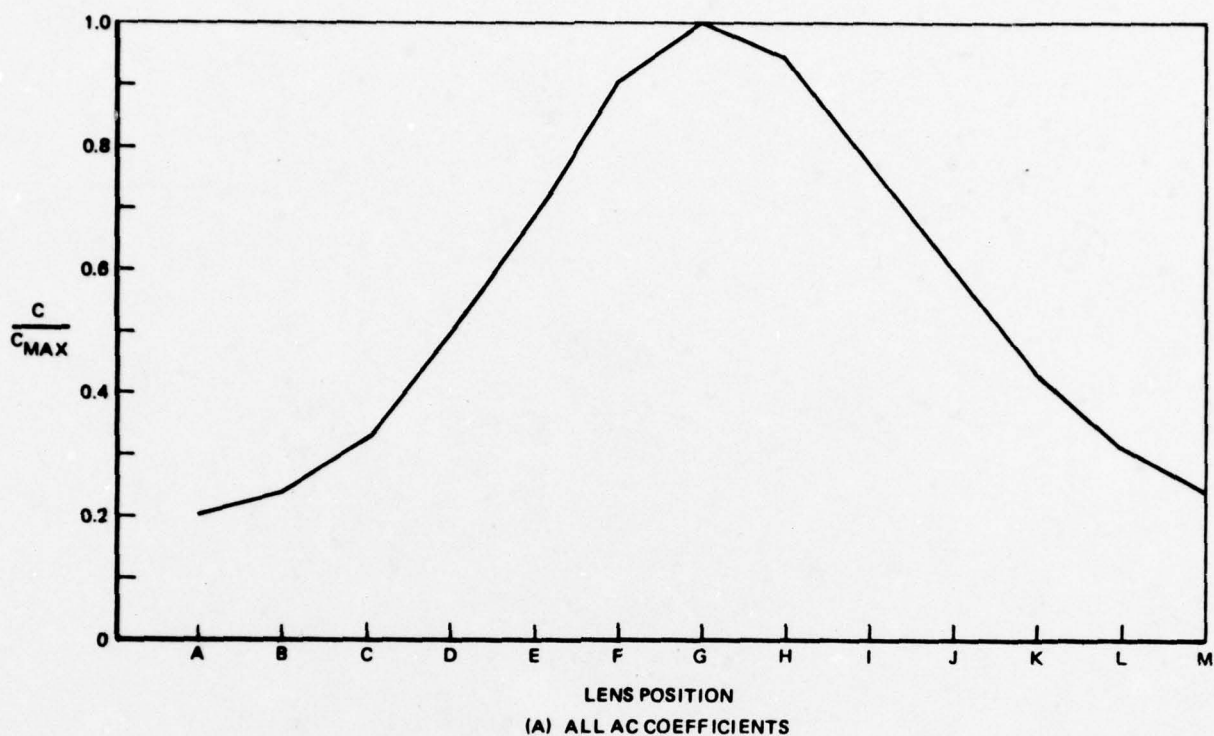
4359

Figure 2-8. C, SUM OF AC POWER, AS A FUNCTION OF LENS POSITION

0.05

0.04

0.03

$$\frac{\text{RMS NOISE}}{\text{RMS } S_M}$$

0.02

0.01

0

1 2 3 4 5 6 7 8 9 10 11 12 13 14 15

GROUP

(A) RMS NOISE VERSUS GROUP

0.02

$$\frac{\text{RMS NOISE}}{\text{RMS } S_M}$$

0.01

0

1 2 AND 3 4-6 7-10 11-15 AC

GROUPINGS

(B) RMS NOISE VERSUS GROUPINGS

4359

Figure 2-9.   RMS NOISE LEVELS FOR S_m, SUM OF AC MAGNITUDES

2-17
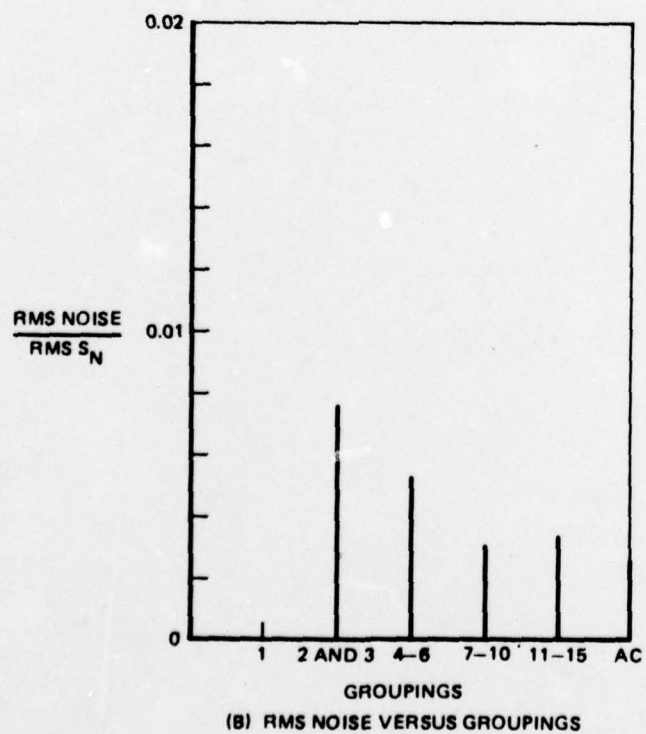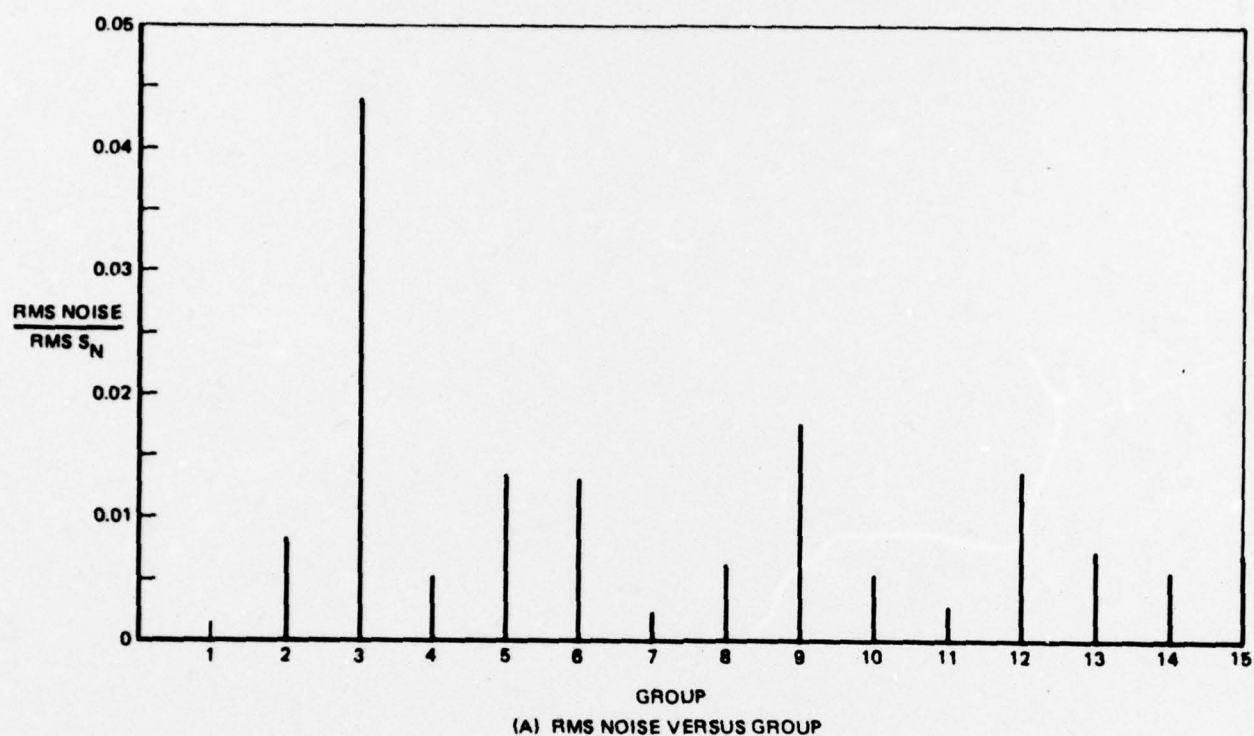
Figure 2-10. RMS NOISE LEVELS FOR S_n, SUM OF NORMALIZED AC MAGNITUDES
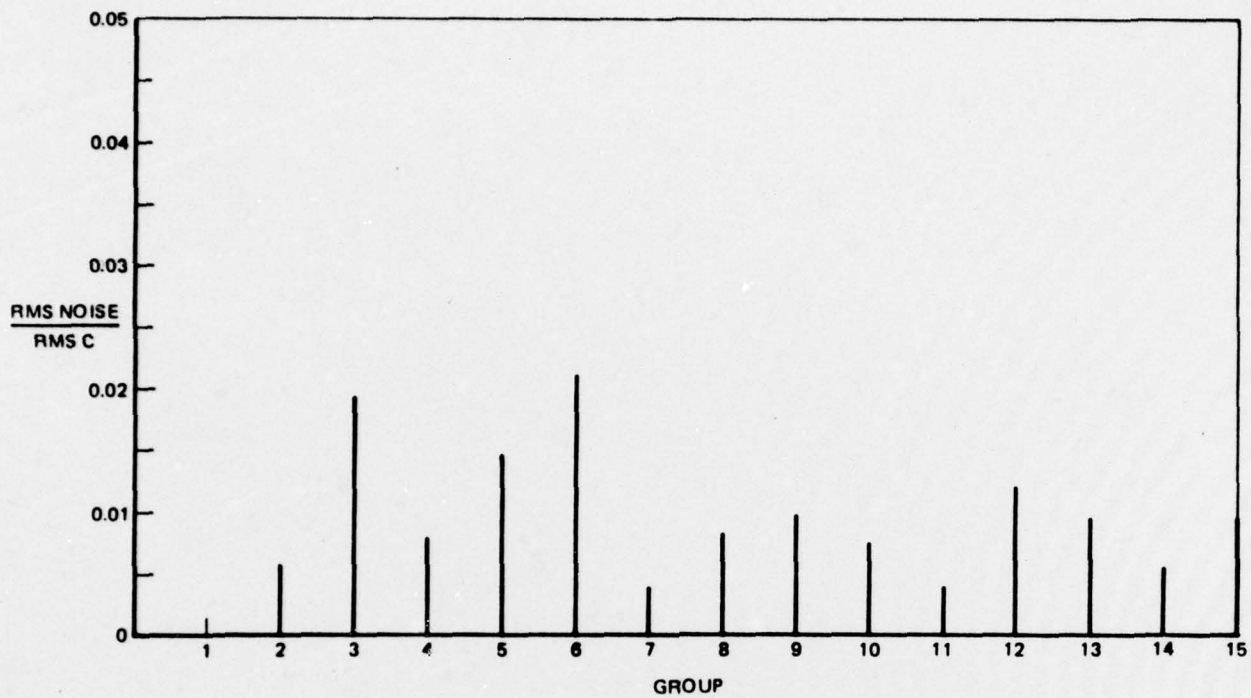
(A) RMS NOISE VERSUS GROUP
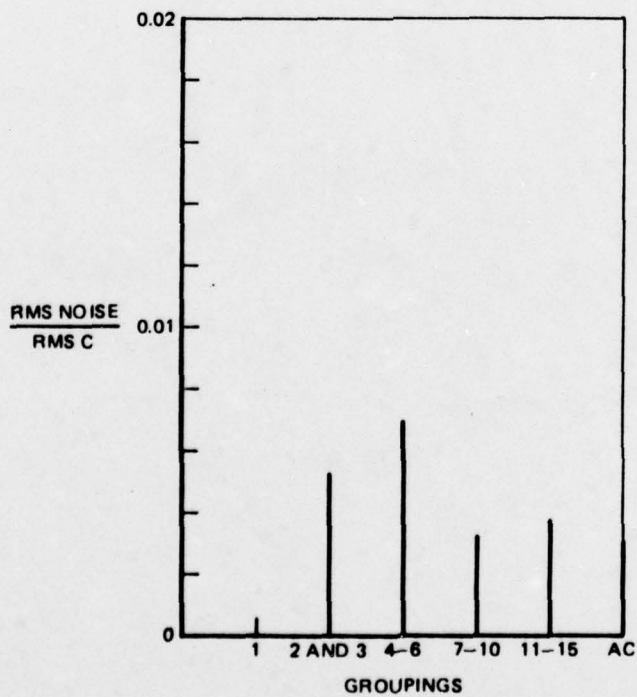
(B) RMS NOISE VERSUS GROUPINGS

4359

Figure 2-11. RMS NOISE LEVELS FOR C, SUM OF AC POWER
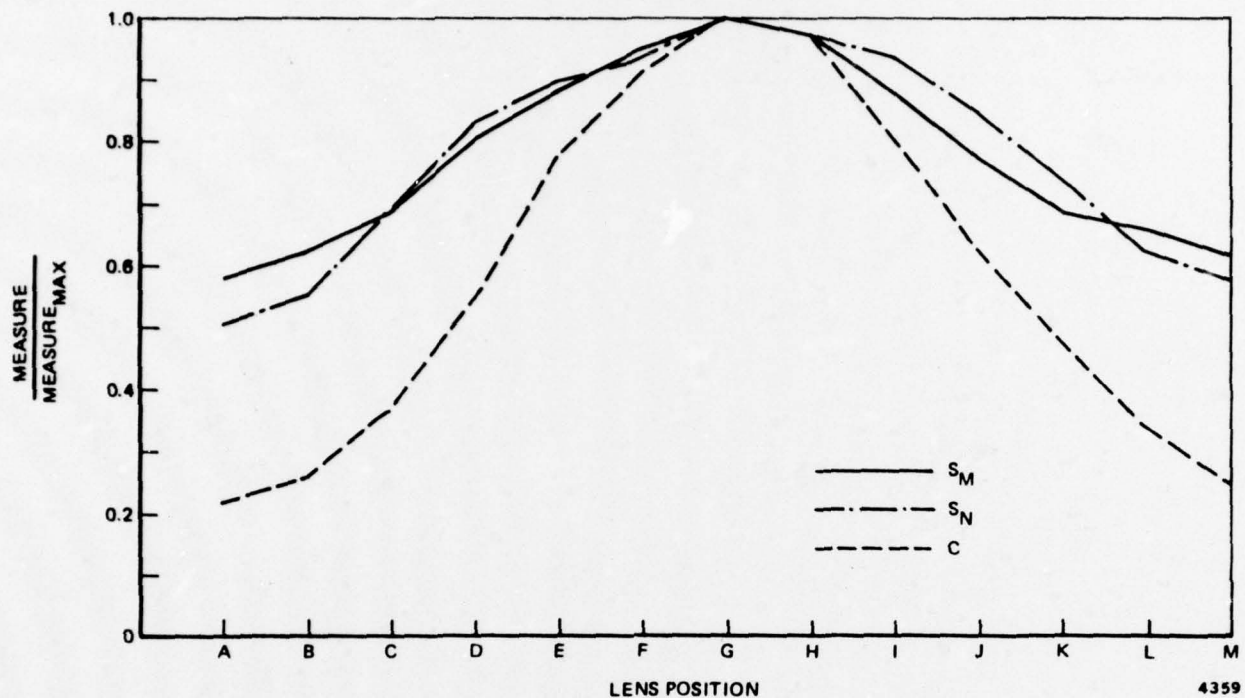
Figure 2-12. A COMPARISON OF FOCUS MEASURES

ly flat, its performance being only slightly poorer at its end points than that of the sum of the normalized magnitudes of the ac coefficients. The relative insensitivity exhibited by these two curves is due to the uniform weighting of each coefficient within any sequency group. When any set of numbers is summed in this fashion, a substantial change in a few members of the set often is obscured by effectively averaging them with the others. By squaring the numbers before summing them, however, the sensitivity to small changes may be increased. This increased sensitivity is exhibited in Figure 2-12 by the curve for the ac power contained in the image's Haar transform.

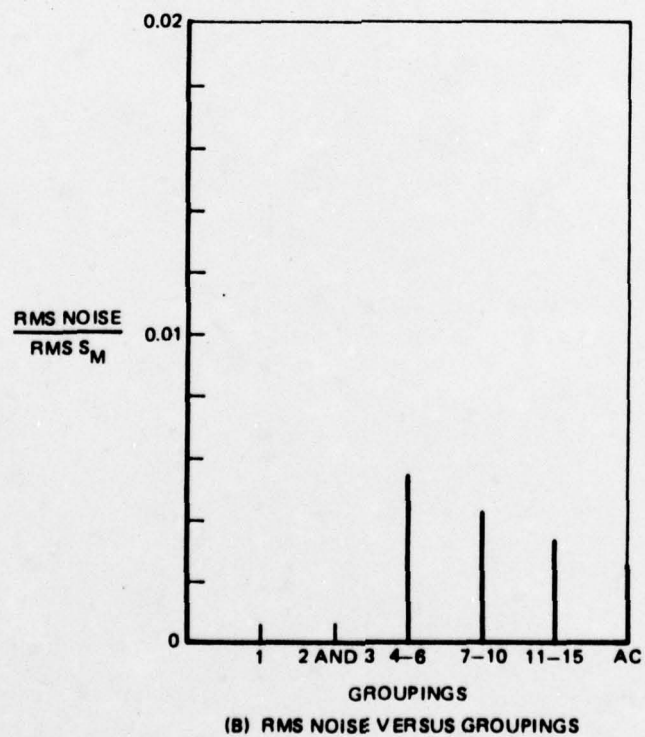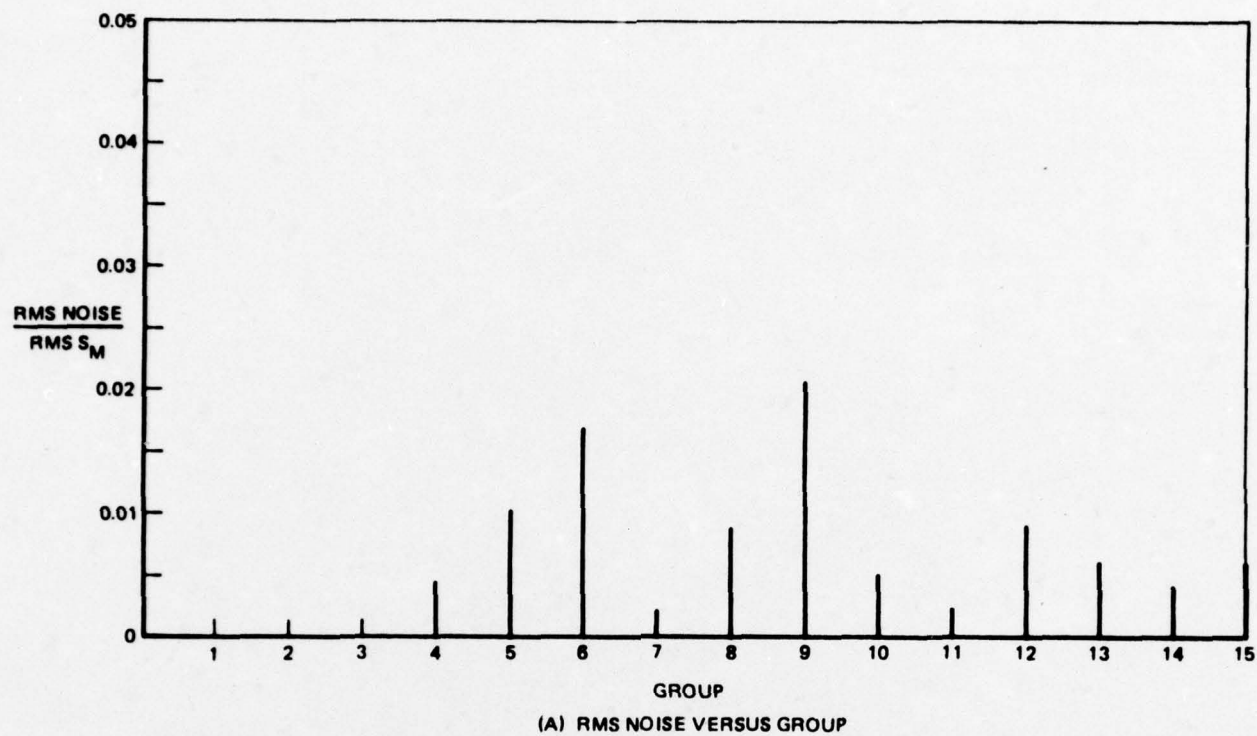Examination of the noise characteristics of each focus measure (Figures 2-9, 2-10, and 2-11) shows that their noise levels, expressed as a fraction of peak value, are roughly equivalent. By assuming the maximum observed value of a focus measure minus its minimum value to be the available signal, the signal-to-noise ratio can be determined. The signal-to-noise ratios of the first three focus measures are shown in Table 2-1. As expected, C, the ac power of the image's Haar transform, has the highest signal-to-noise ratio.

2-20

Table 2-1. FOCUS MEASURE SIGNAL-TO-NOISE RATIOS

Focus Measure	Signal-to-Noise Ratio (dB)
S_m, Sum of AC Magnitudes	43
S_n, Sum of Normalized AC Magnitudes	44
C, AC Power	49

The behavior of texture and edge activity as a function of lens position was deter-
mined in a fashion similar to the other focus measures, i.e., evaluating the focus
measure at each point through one lens cycle. However, the area of the test pattern
for which the descriptors were computed was different than that used for the other
measures. Figure 2-13 shows the test pattern with the descriptor input areas flagged
by increased brightness. These areas were chosen so that texture and edge would be
computed for both the center of the image, which is primarily texture, and the
borders of the image, which are composed primarily of two singular edges.

The computed values of texture activity, edge activity, and their sum are shown as
a function of lens position in Figure 2-14. As depicted in Figure 2-14, edge activ-
ity behaves much like ac power. Texture activity, however, exhibits markedly dif-
ferent characteristics. While similar to the other curves in having a peak at lens
position G, the texture activity curve also has a local minimum at lens position C.
The precise effect that defocusing an image has on the division of activity into
texture and edge information is not yet fully understood.

The computational complexity of each of the focus measures is tabulated in Table
2-2. The computation time of each measure is the time required for the instrumenta-
tion system's minicomputer to evaluate the state of focus of one 16 by 16 pel block
of the image. The minicomputer (Computer Automation LSI-2) has an average instruc-
tion cycle time of 1 μsec. System overhead operations are not included in the com-
putation time values.

As shown in Table 2-2, S_m is the simplest measure to compute as it evolves only 254
additions operations. S_n requires 190 power of two multiplications (shifts) as
well as the additions operations. In order to compute C, the total ac power of the
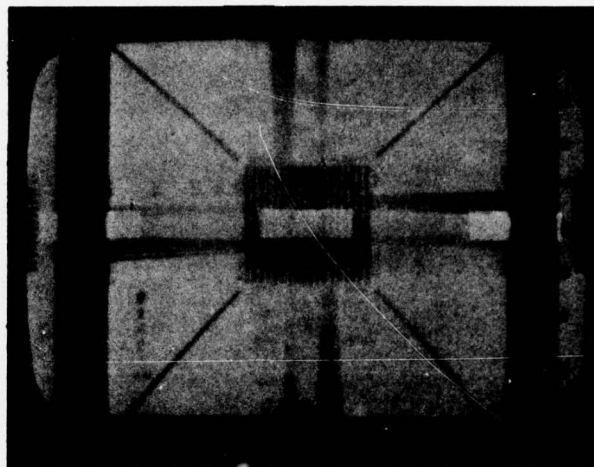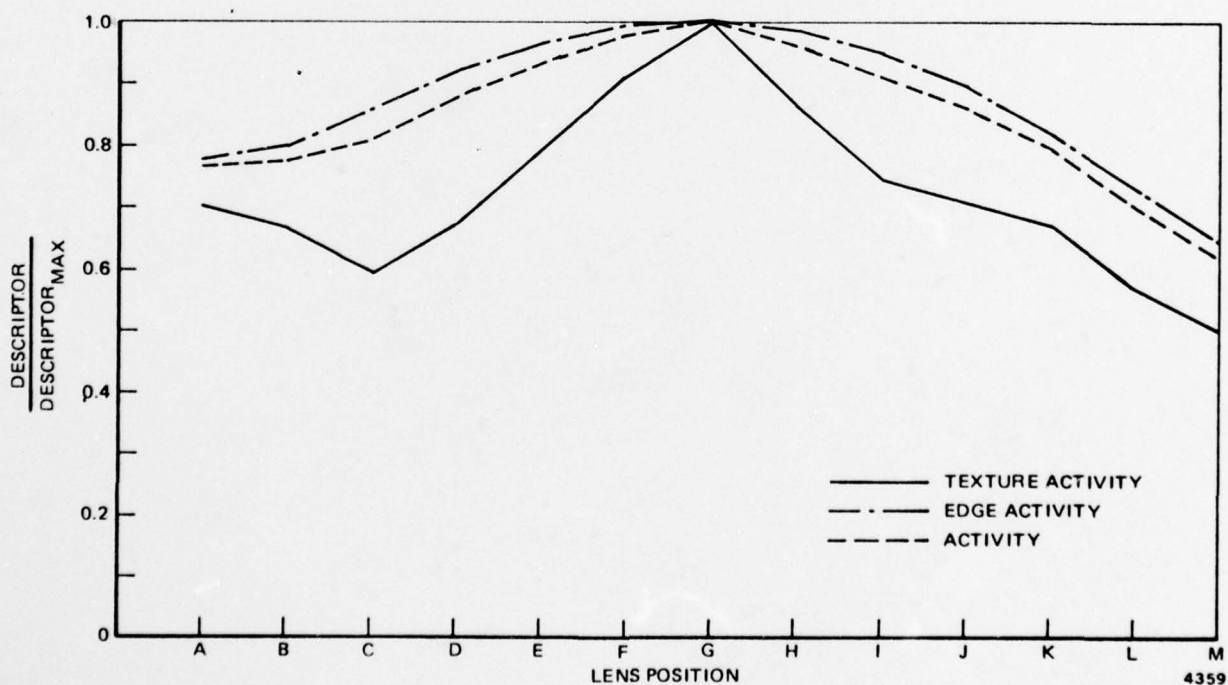
Figure 2-13.   TEST PATTERN DESCRIPTOR INPUT AREAS

Figure 2-14.   ACTIVITY DESCRIPTORS AS A FUNCTION OF LENS POSITION

Table 2-2. FOCUS MEASURE COMPUTATIONAL COMPLEXITY

Measure	Computation Time	Real Time Compatibility
S_m, Sum of AC Magnitudes	254 µsec	Excellent
S_n, Sum of Normalized AC Magnitudes	464 µsec	Good
C, Total AC Power	765 µsec	Good
Texture and Edge Activity	~204 msec	Very Poor

16 by 16 pel block, each of the 255 ac coefficients must be squared before summation occurs. Because of the LSI-2's arithmetic format, squaring, or simple integer multiplication, uses two computer instruction cycles. The number of cycles required to compute C then is (255 x 2) + 254 = 765.

Unlike the previous three focus measures, which involve integer arithmetic, texture and edge activity require the use of floating point arithmetic. As a consequence, not only is the number of requisite instruction cycles much greater for each operation, it is data dependent as well. The computation time for texture and edge activity listed in Table 2-2 is the time observed for the computation of these measures, scaled down by an estimate of percent system overhead. The texture and edge activity focus measure is clearly not compatible with a real-time system.

2.3.3 Summary

The performance of each focus measure in evaluating the state of focus of the video test pattern is summarized in Table 2-3.

Of the measures studied, the total ac power provides the focus measure with the best sensitivity to focus and the highest signal-to-noise ratio. The only disadvantage associated with using ac power as a measure of focus is that, compared to S_m and S_n, it is relatively expensive to compute. In terms of TV frame rates, however, its performance is still acceptable. For example, the ac power of about forty 16 by 16 pel image blocks could be computed during the elapsed time of one TV frame.

Table 2-3. PERFORMANCE OF CANDIDATE FOCUS MEASURES

Measure	Sensitivity to Focus	Signal-to-Noise Ratio (dB)	Required Computation Time
S_m, Sum of AC Magnitudes	Fair	43	254 μsec
S_n, Sum of Normalized AC Magnitudes	Fair	44	464 μsec
C, AC Power	Good	49	756 μsec
Texture vs Edge	Poor	--	204 msec

The measures of focus to be evaluated on the NVL FLIR imagery in the next experi-
ment are C, the total ac power or image activity, and X and E, the texture and edge
activities of the image. C was selected for its superior performance on the video
test pattern. Texture and edge activity are being evaluated further to determine
their behavior on images that are of a more general nature than the video test
pattern.

2.4 FLIR IMAGE EXPERIMENT

In order to ascertain the ability of ac power to discriminate focus on FLIR imagery,
the five FLIR images supplied by NVL were used as input data in the test configura-
tion shown in Figure 2-1. In each image, areas containing only background and
areas containing both background and target information were considered. For the
background data, the ac power of three fixed sets of eight 16 by 16 pel blocks was
evaluated. These input areas are flagged by increased brightness in Figure 2-15.
Target data were collected by restricting the input data to only the sector(s) that
contained one of the targets in the image under consideration.

In each case, the ac power of the image input area was evaluated through four lens
cycles and the results averaged for graphical presentation.
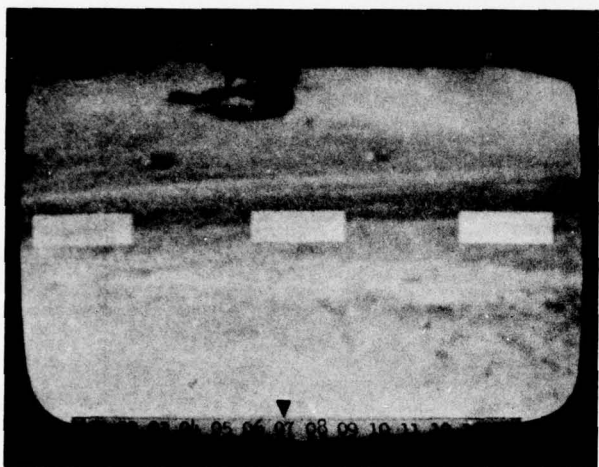
(A)   IMAGE 1
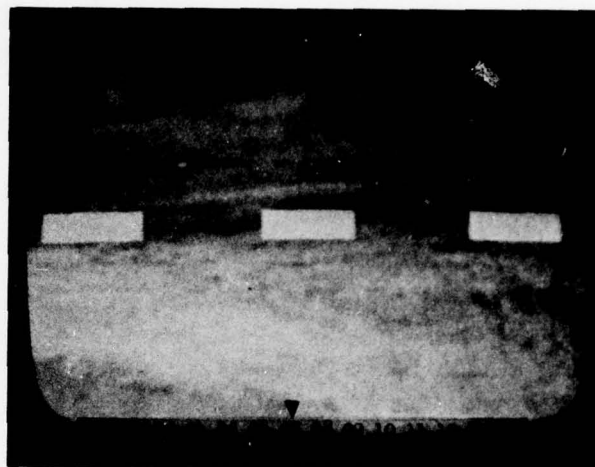
(B)   IMAGE 2

(C)   IMAGE 3

(D)   IMAGE 4

Figure 2-15.   FLIR IMAGES WITH INPUT AREAS FLAGGED BY INCREASED BRIGHTNESS
(Sheet 1 of 2)

(E)   IMAGE 5

Figure 2-15.   FLIR IMAGES WITH INPUT AREAS FLAGGED BY INCREASED BRIGHTNESS
(Sheet 2 of 2)

2.4.1 Image Data

The variations in ac power as a function of lens position are shown in Figures 2-16 through 2-21 for background data, and in Figures 2-22 through 2-26 for target data.
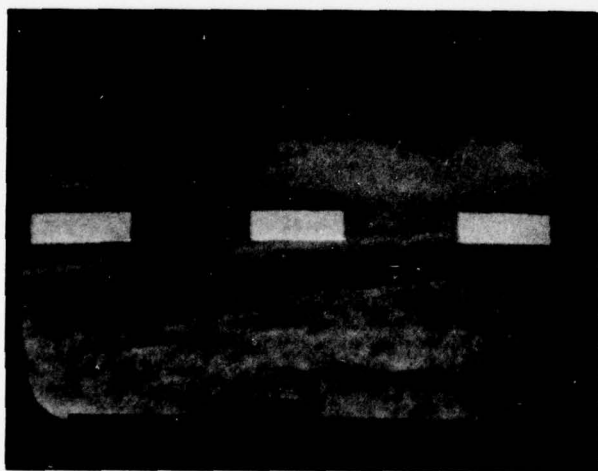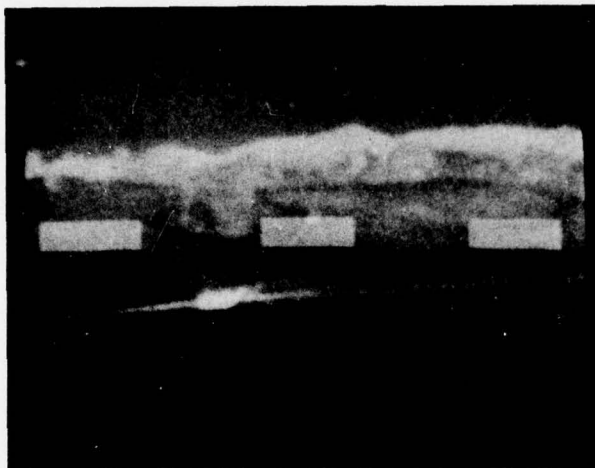
As can be seen in Figures 2-16 through 2-21, the background data curves are relatively insensitive to focus. The curve for Image 5 (Figure 2-20), as a worst case example, is almost completely insensitive to changes in lens position. This effect is due primarily to the lack of activity in the input sectors of the image.

By choosing an alternate set of input sectors for Image 5 and evaluating the resultant fluctuations in ac power, a curve whose sensitivity to focus is comparable to those of the other images is obtained (Figure 2-21). The alternate sectors used are those immediately above the ones shown in Figure 2-15. The average activity increase obtained by moving the input areas in this instance is 33 percent. The central input area experiences a two-fold increase in activity.

The curves relating to the state of focus of the targets (Figures 2-22 through 2-26) exhibit an increased sensitivity to focus when compared to the background curves. This improvement in sensitivity is, again, primarily due to the increased

2-26
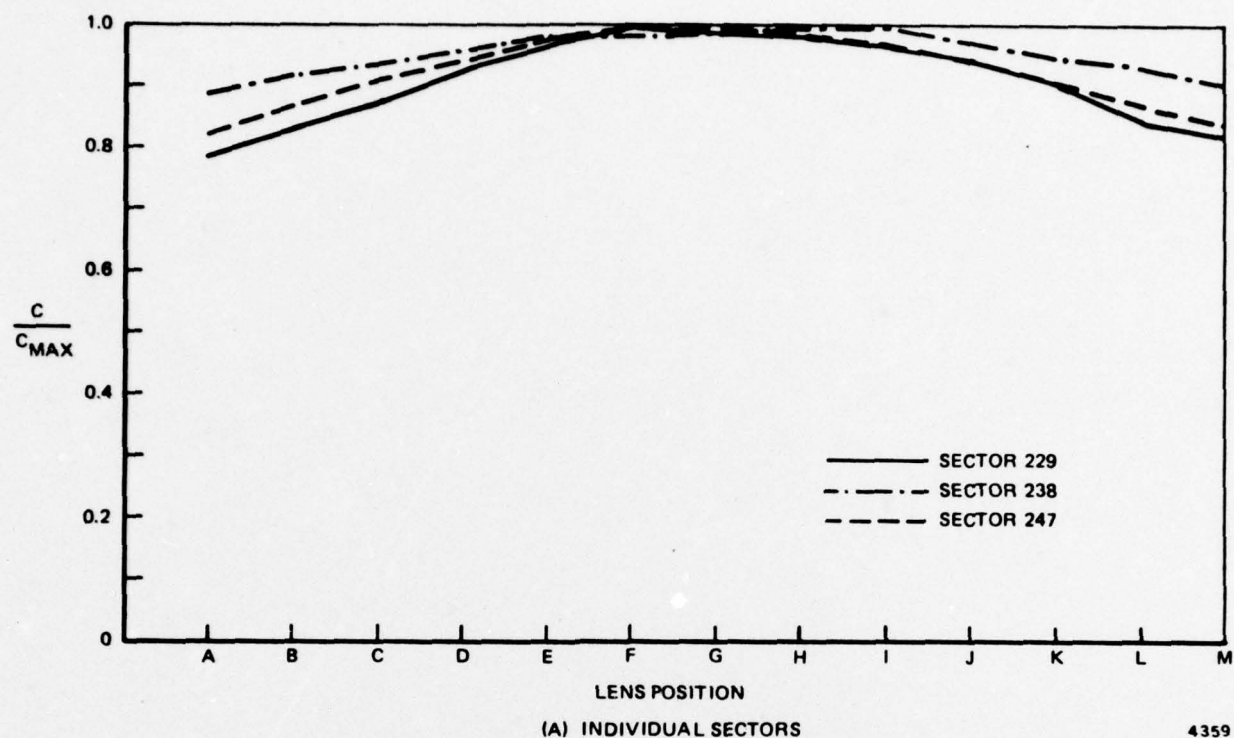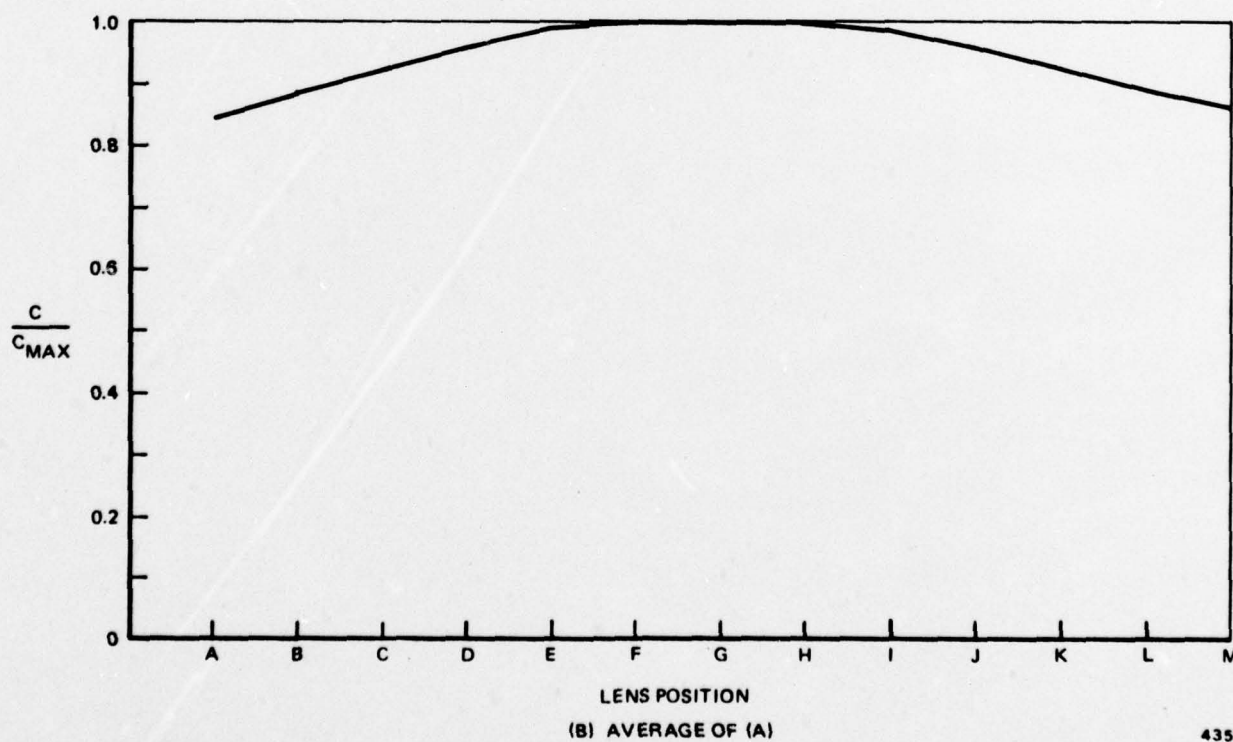
Figure 2-16.   TOTAL AC POWER - IMAGE NO. 1

Figure 2-17.   TOTAL AC POWER - IMAGE NO. 2

Figure 2-18. TOTAL AC POWER - IMAGE NO. 3

Figure 2-19.   TOTAL AC POWER - IMAGE NO. 4
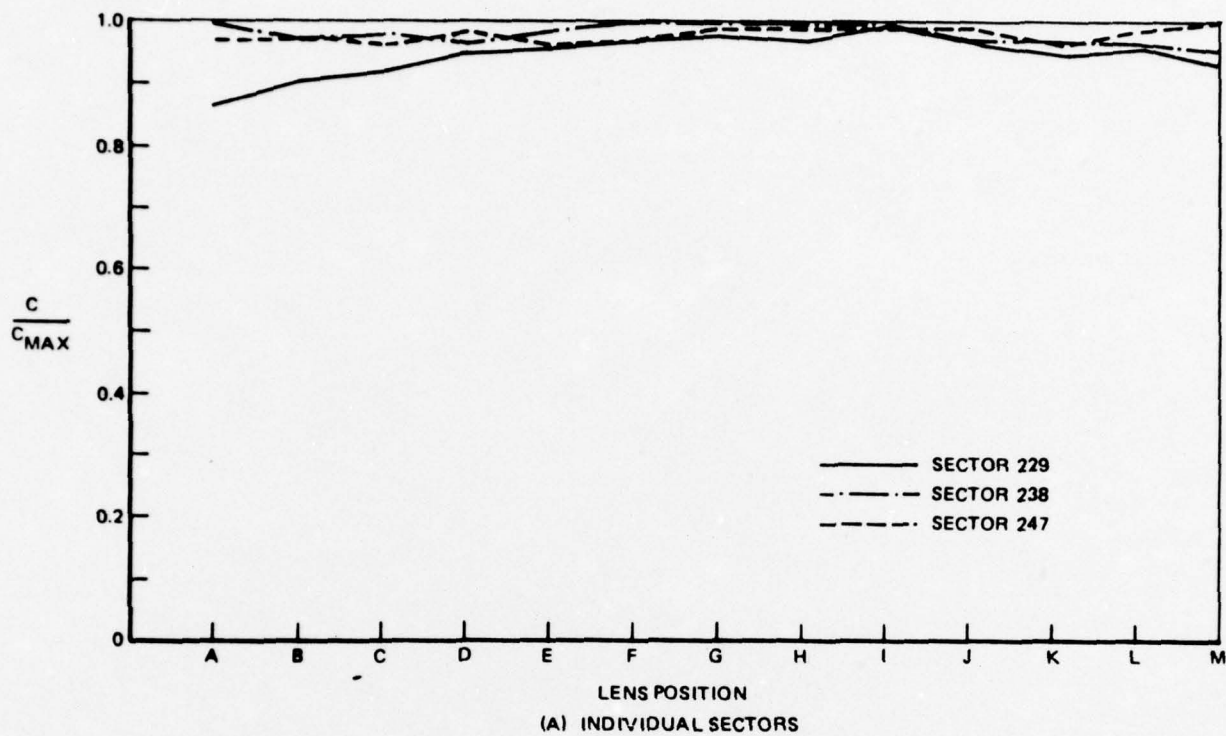
Figure 2-20. TOTAL AC POWER - IMAGE NO. 5

(A) INDIVIDUAL SECTORS

4359

(B) AVERAGE OF (A)

4359
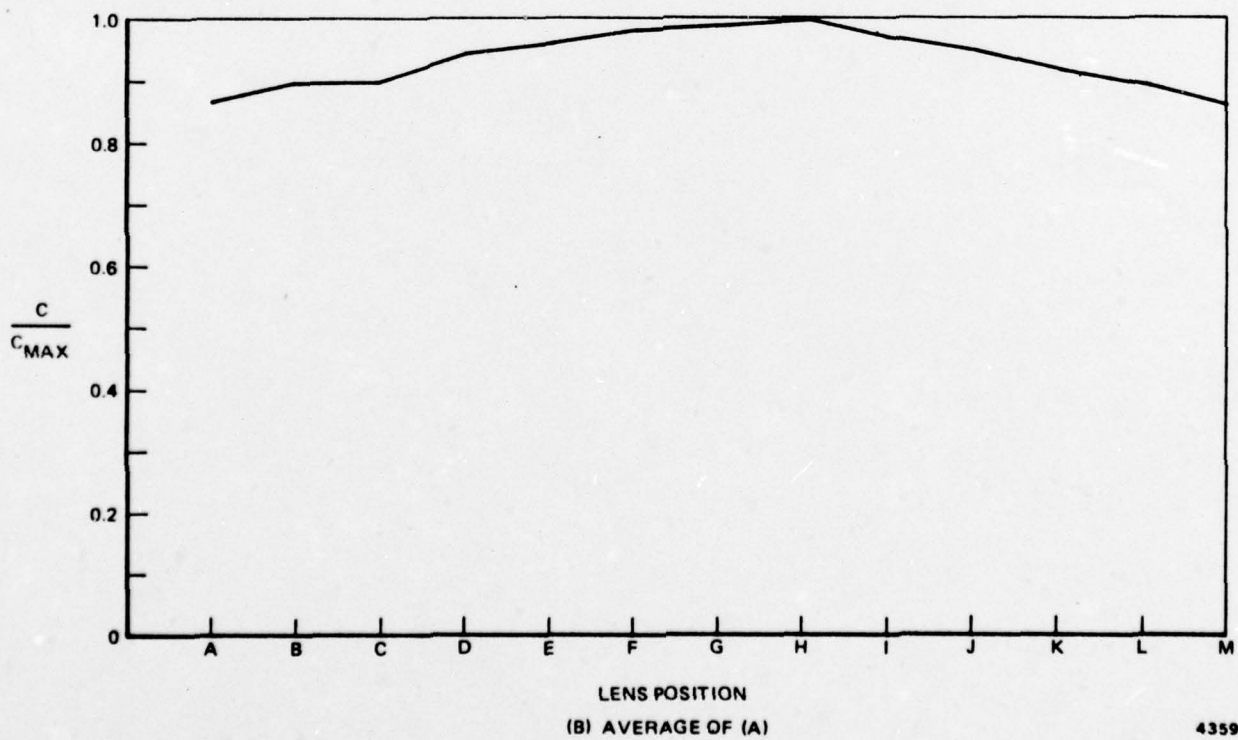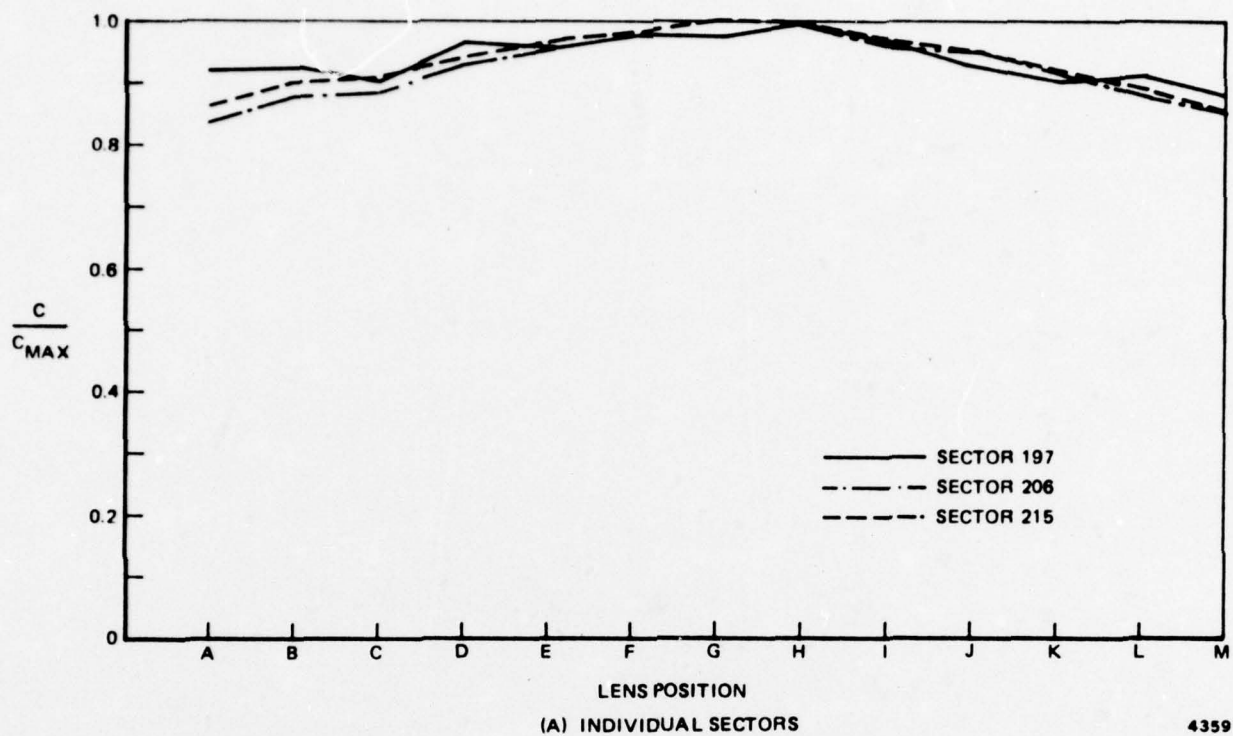
Figure 2-21. TOTAL AC POWER - IMAGE NO. 5 (ALTERNATE SECTORS)
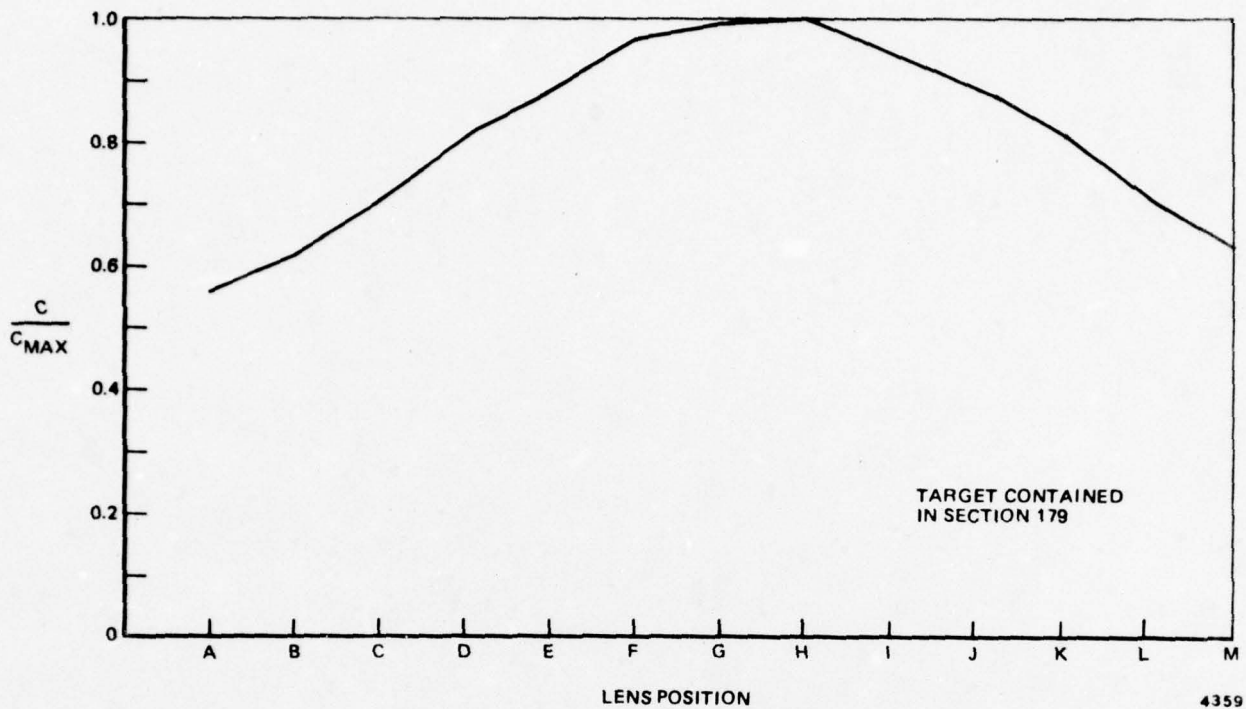
Figure 2-22. TOTAL AC POWER - IMAGE NO. 1 TARGET
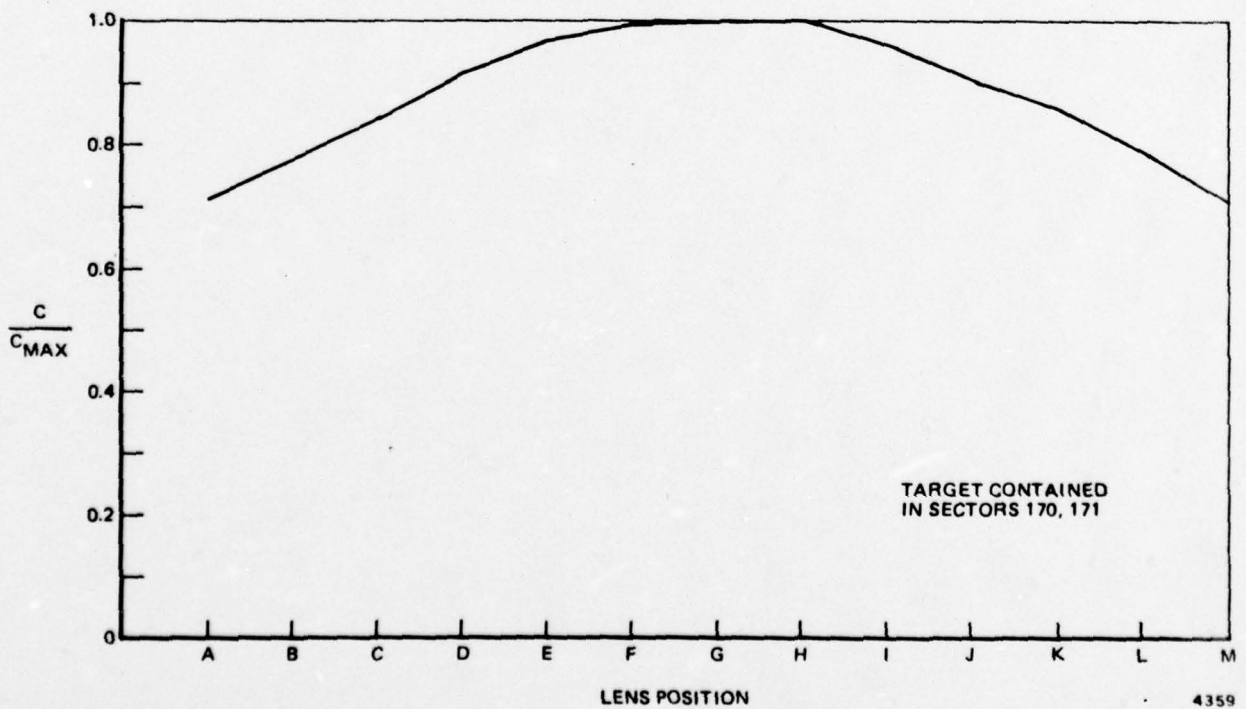
Figure 2-23. TOTAL AC POWER - IMAGE NO. 2 TARGET
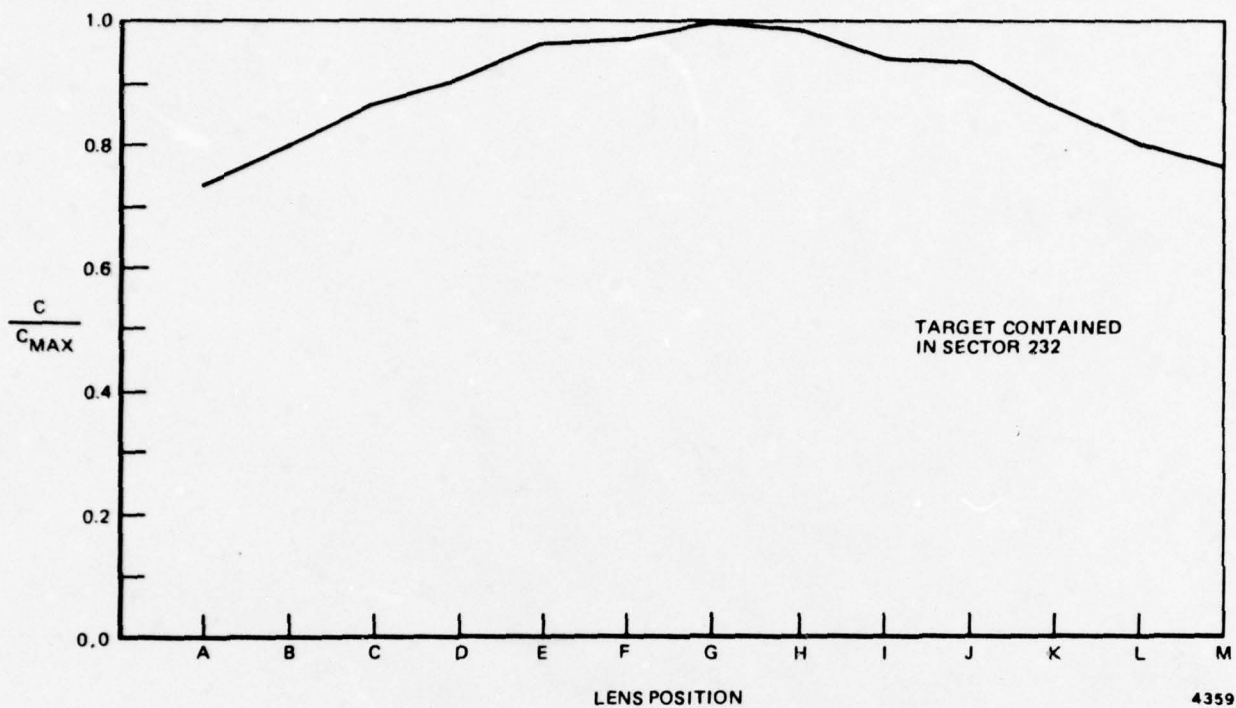
Figure 2-24. TOTAL AC POWER - IMAGE NO. 3 TARGET
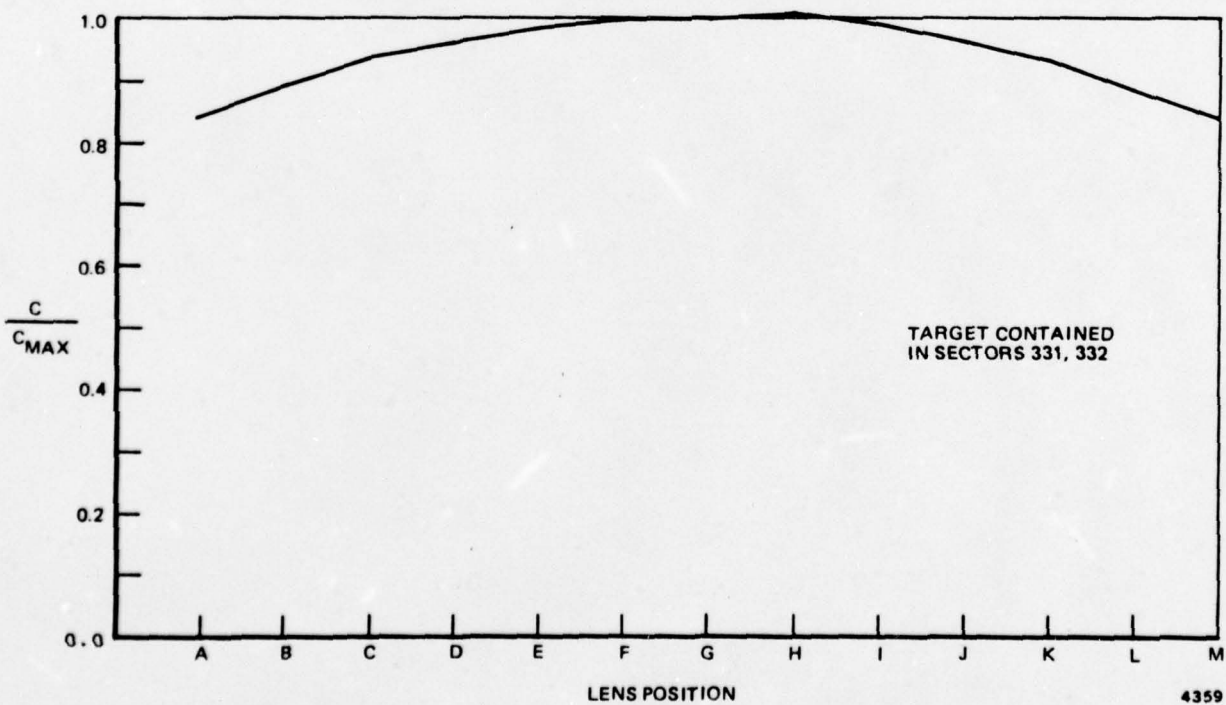
Figure 2-25. TOTAL AC POWER - IMAGE NO. 4 TARGET

$\frac{c}{c_{MAX}}$

1.0

0.8

0.6

0.4

0.2

0.0

A   B   C   D   E   F   G   H   I   J   K   L   M

LENS POSITION

TARGET CONTAINED IN SECTORS 299, 300, 301

4359
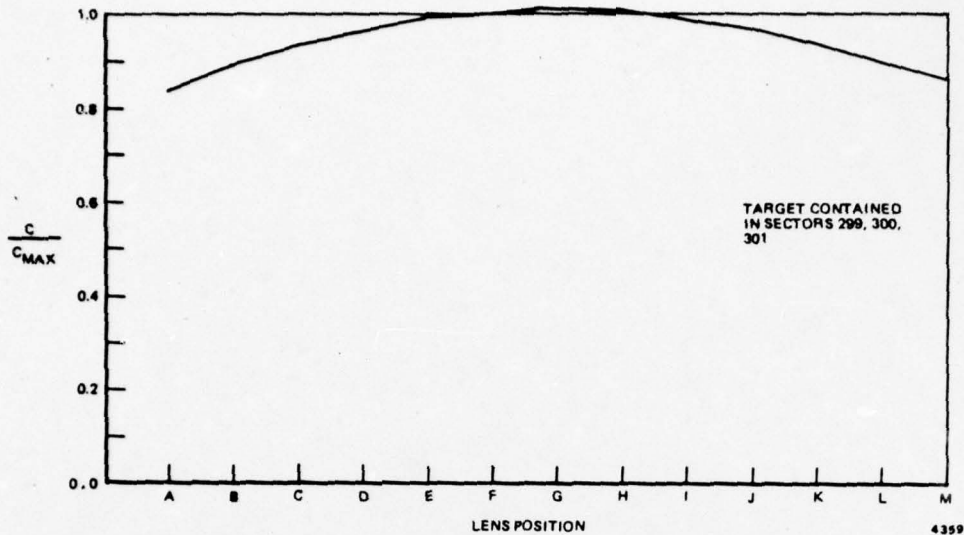
Figure 2-26.   TOTAL AC POWER - IMAGE NO. 5 TARGET
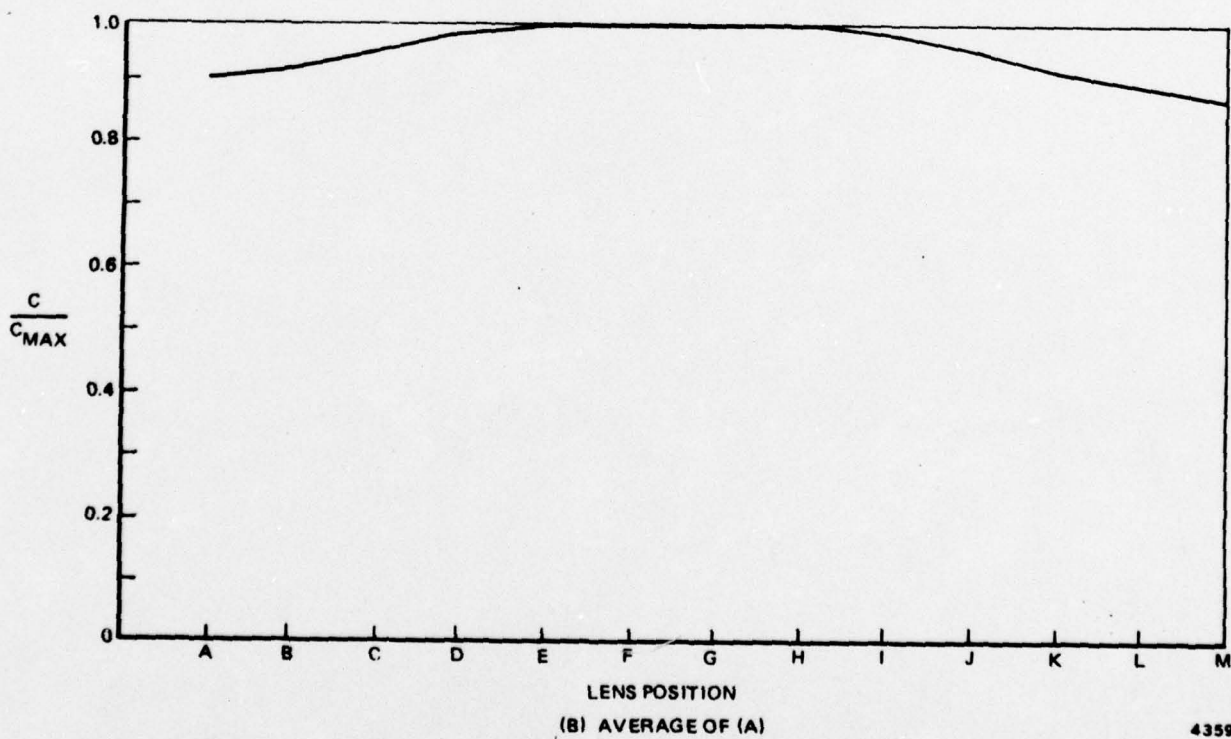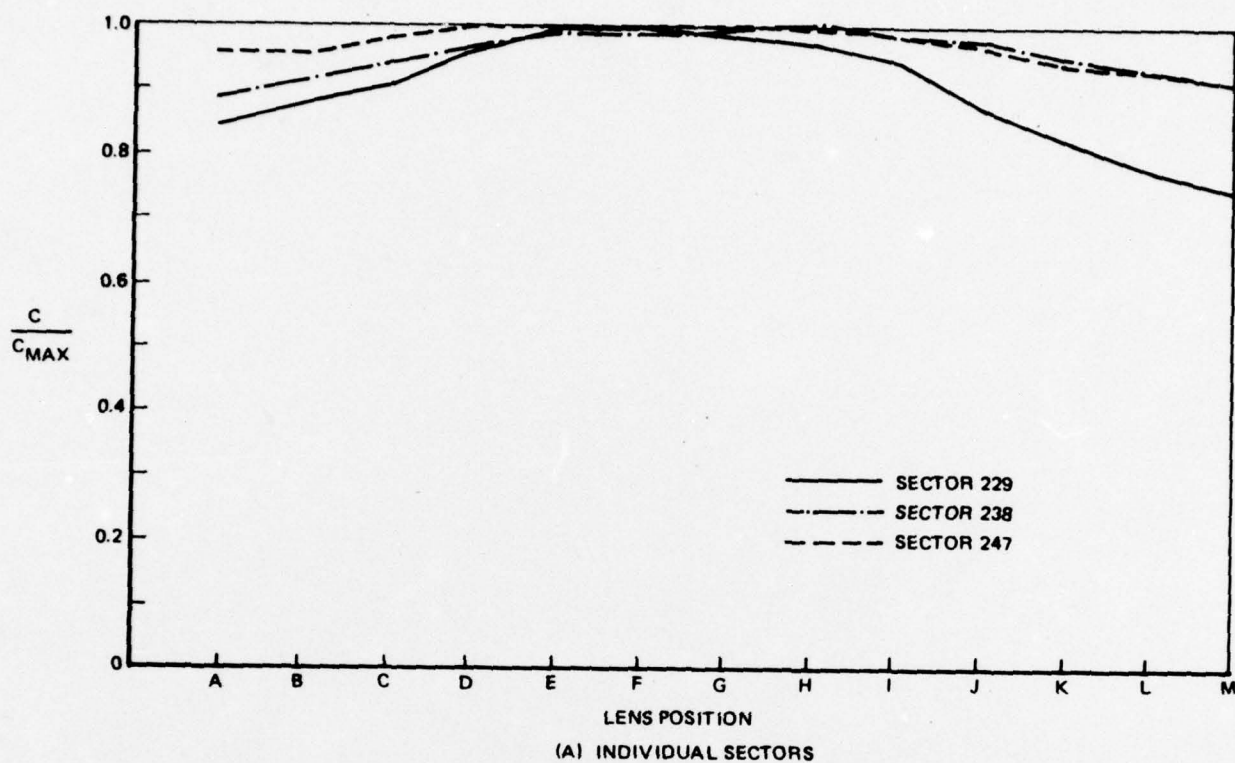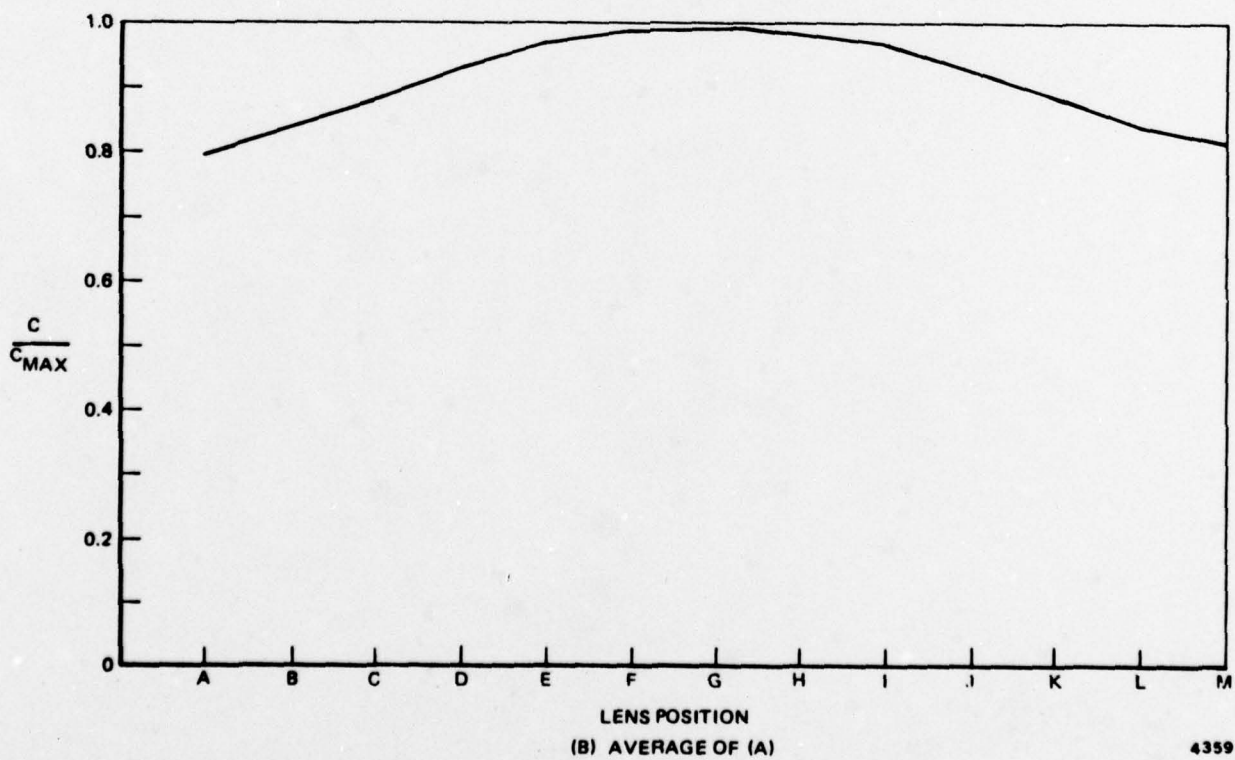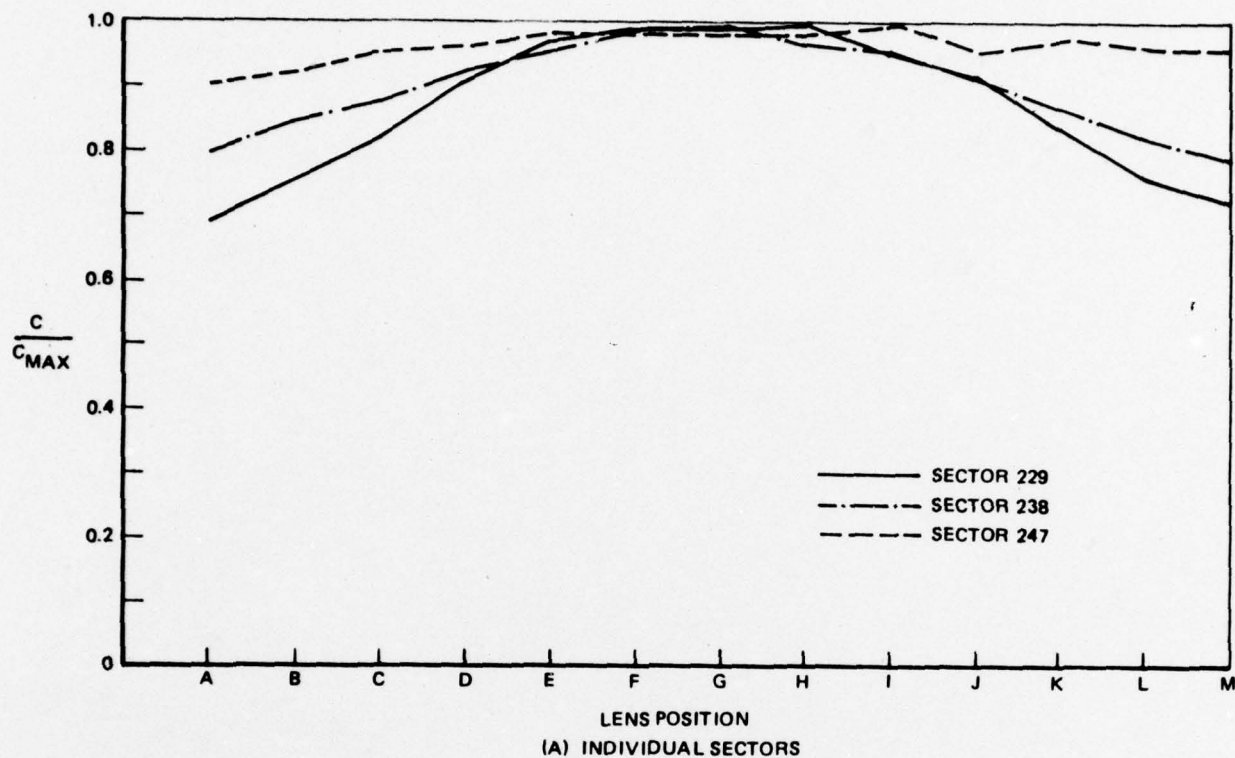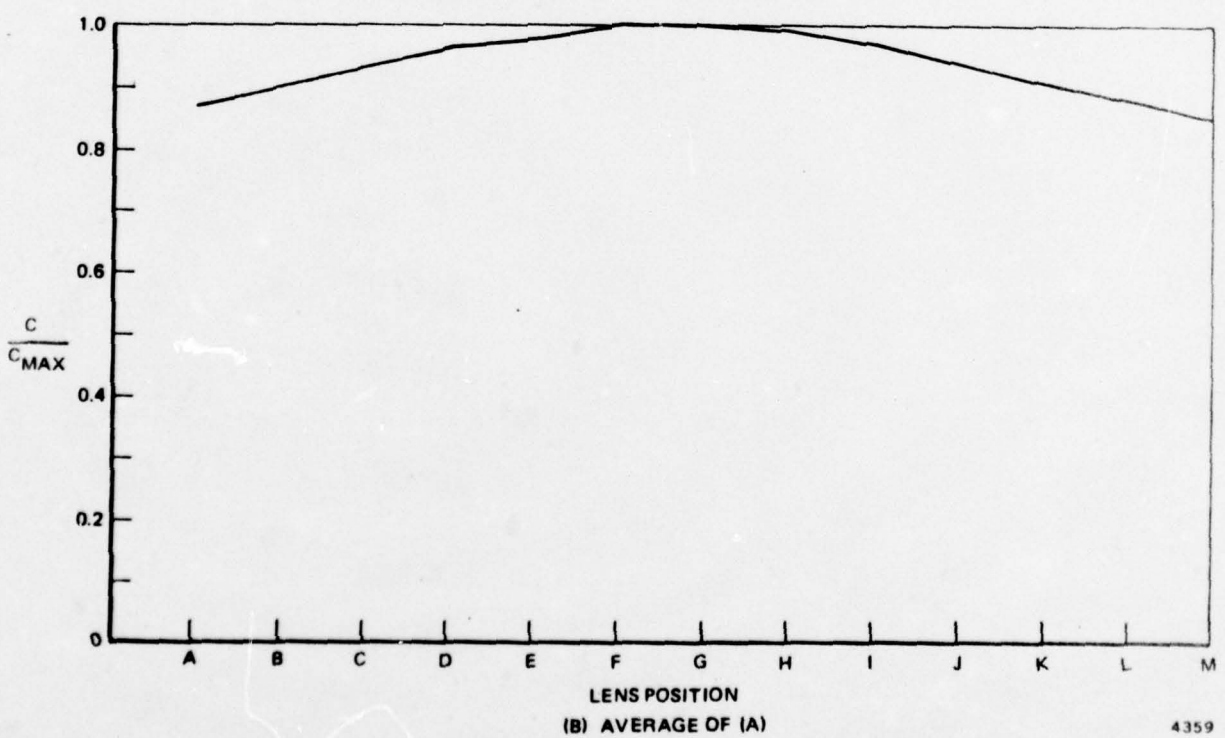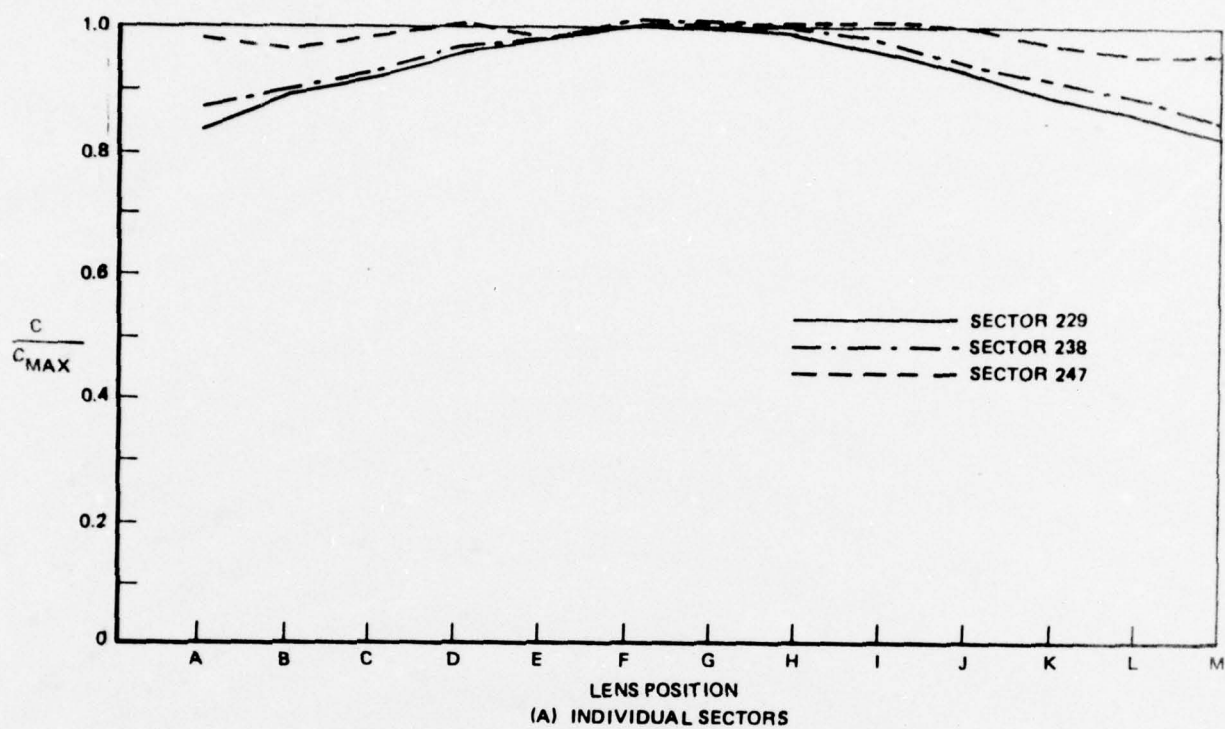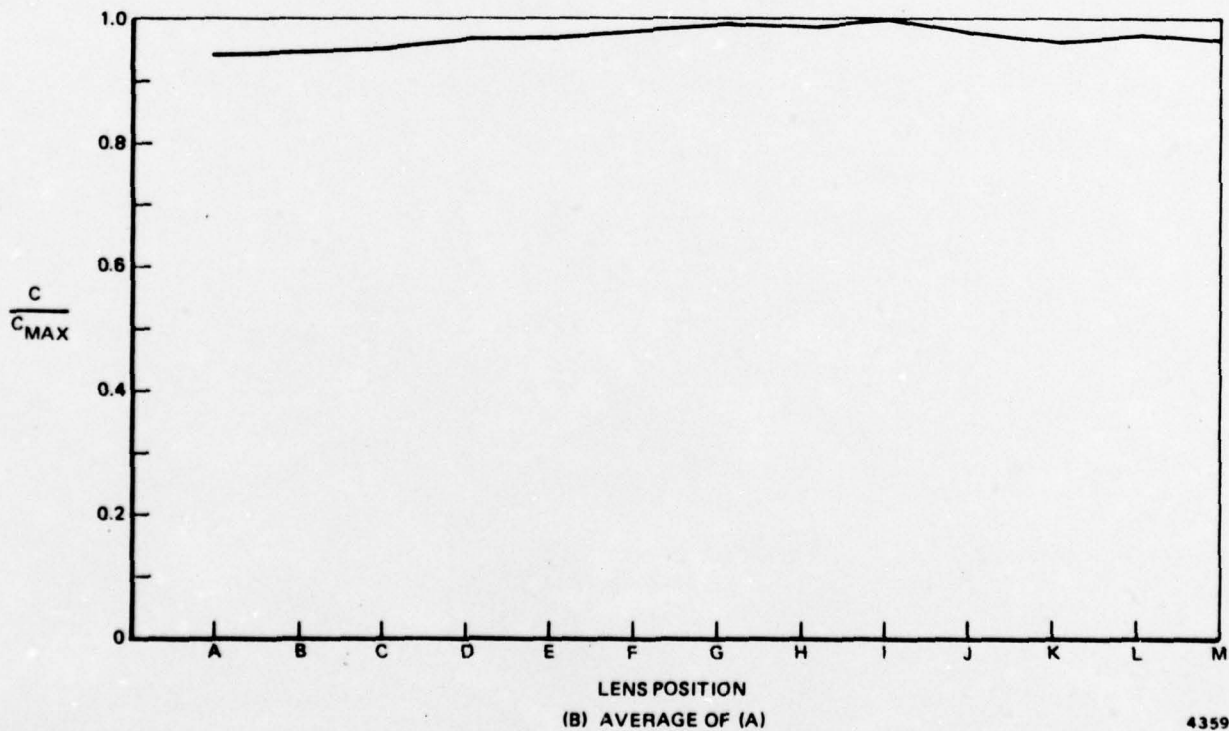
activity of the target sectors. The ac power of the target sectors is about twice that of the average background sector. The target curves showing the most sensitivity to focus are those from Images 1, 2, and 3. The targets in each of these images are small, detailed, high-contrast objects. Objects of this type appear to provide the best information on which to base a state of focus evaluation.

To determine the effect of focus on the division of ac energy into texture and edge activity, the image descriptors were evaluated on representative areas of selected FLIR images. The test FLIR imagery shown in Figure 2-2 falls into two major groups. One group (Images 1, 2, and 3) exhibits small targets on a relatively bright background, while the other group (Images 4 and 5) consists of larger targets against a relatively dark background. One image from each group (Images 1 and 4) was selected to represent its group for the evaluation of the image descriptors. Both target and background areas of the two images were examined. The background areas are identical to those shown in Figure 2-15. For target input information, a 3 by 4 block of image sectors was centered about one of the targets in each image.

The curves relating the behavior of texture and edge activity as a function of lens position are shown in Figures 2-27 through 2-30. It can be seen that while texture and edge activity show approximately the same sensitivity to focus, regardless of the type of input data, the texture curve is much noisier. Averaging the values of texture activity over several lens cycles would probably reduce this noise level substan-

2-35
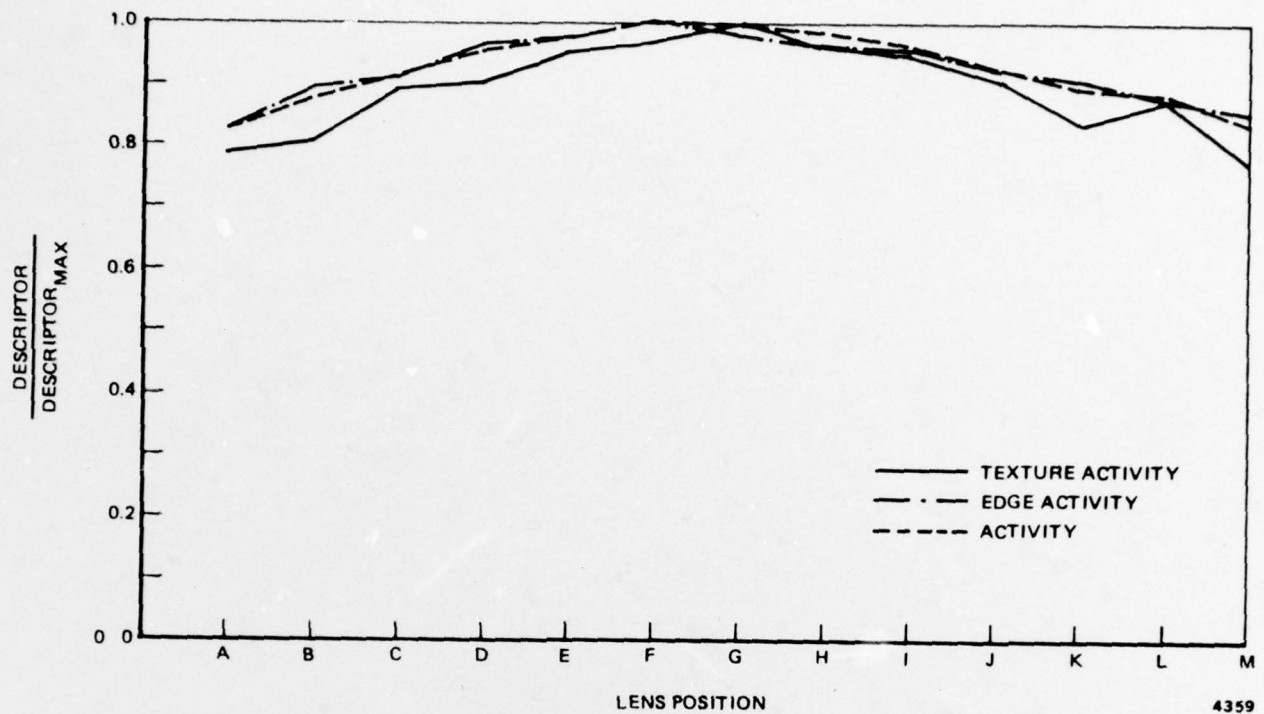
Figure 2-27. ACTIVITY DESCRIPTORS AS A FUNCTION OF LENS POSITION -
IMAGE NO. 1 BACKGROUND
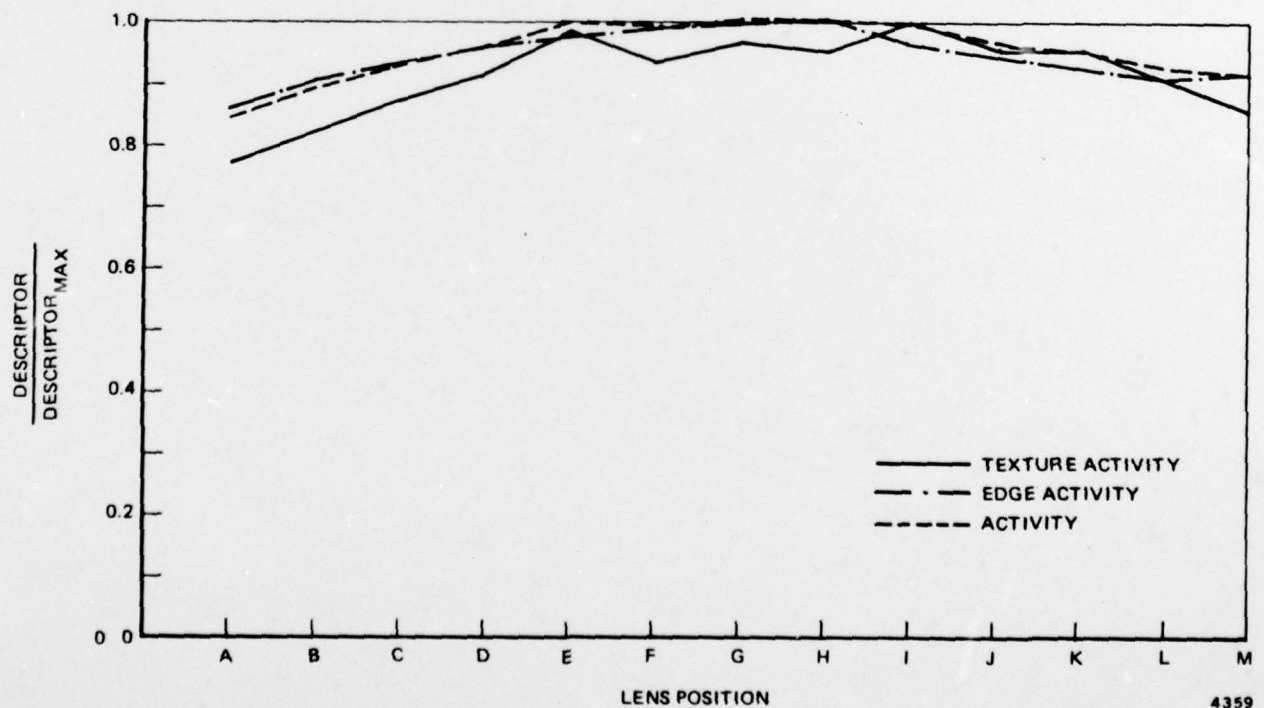
Figure 2-28. ACTIVITY DESCRIPTORS AS A FUNCTION OF LENS POSITION -
IMAGE NO. 1 TARGET

2-36
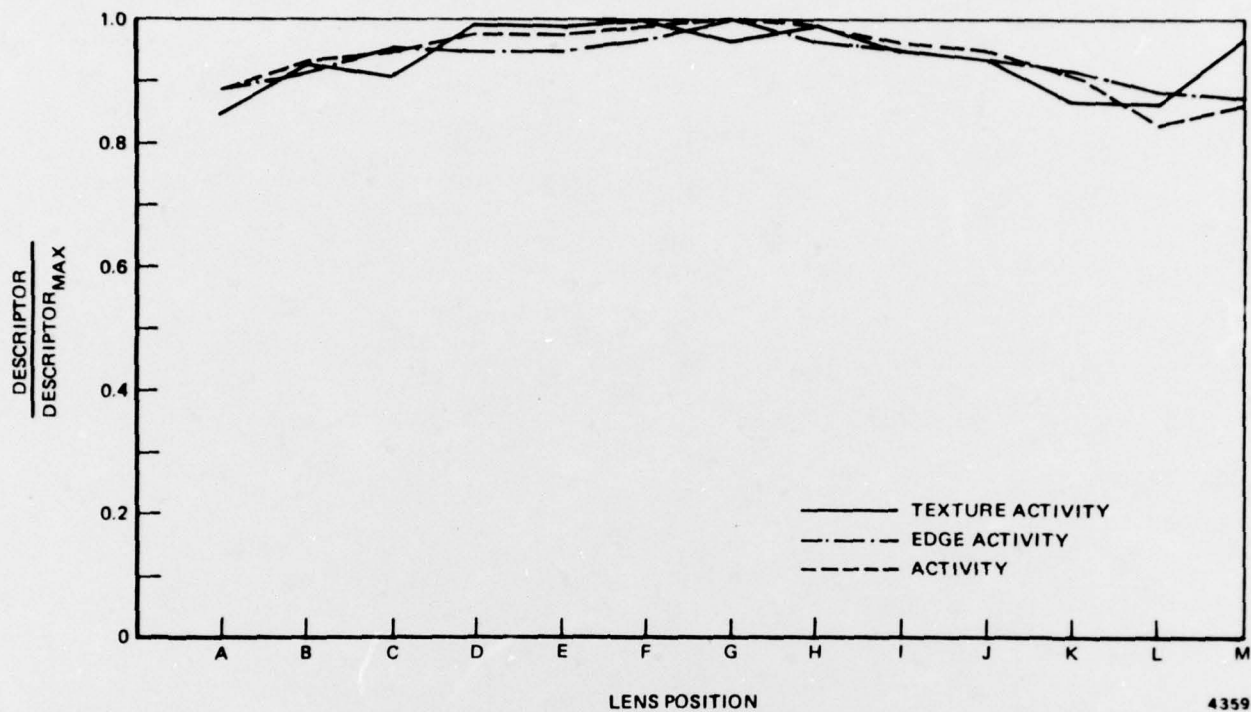
Figure 2-29. ACTIVITY DESCRIPTORS AS A FUNCTION OF LENS POSITION –
IMAGE NO. 4 BACKGROUND
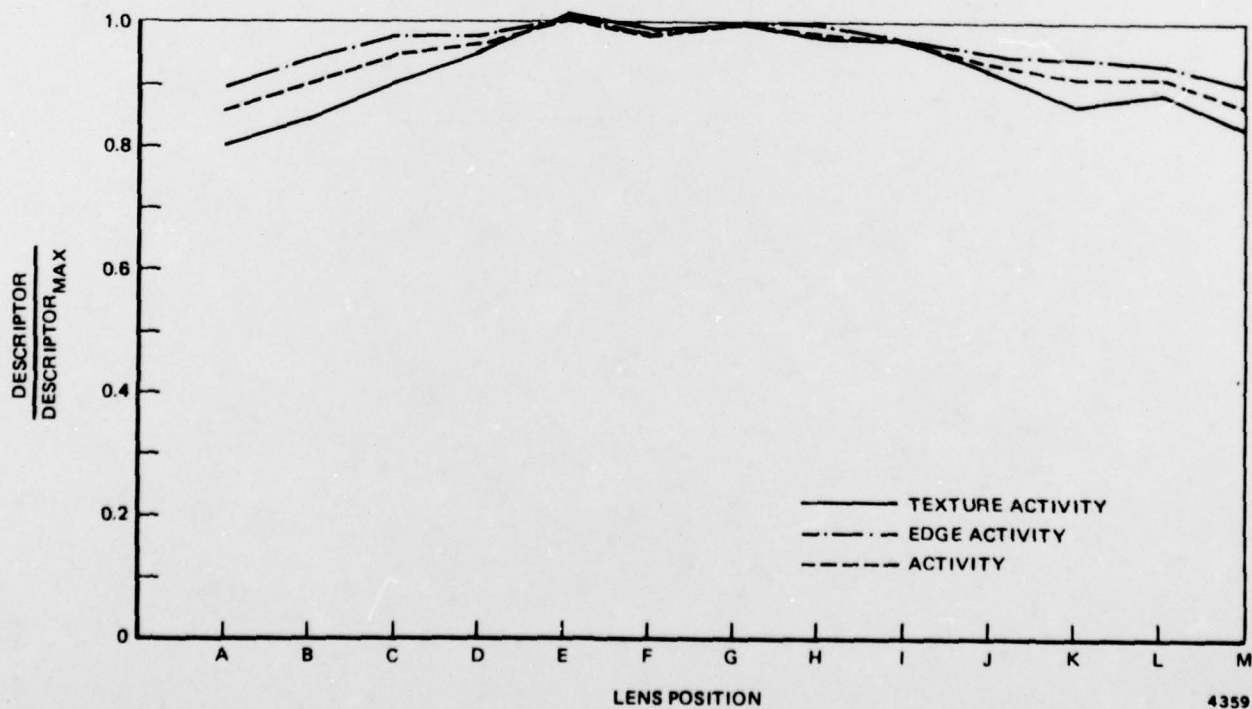
Figure 2-30. ACTIVITY DESCRIPTORS AS A FUNCTION OF LENS POSITION –
IMAGE NO. 4 TARGET

2-37

tially, but the increase in computation time for such an approach would be prohibitive in a real-time system. For the background type data seen in the sample FLIR images provided by NVL, the division of activity into texture and edge information provides little to no additional information about the image's state of focus.

2.4.2 Summary of FLIR Image Experiments

The ac power of selected image sectors can provide a useful index of the state of focus of a FLIR image. The sensitivity of the measure is less for the FLIR images than that seen on the test pattern, but is still sufficient to form the basis of an error signal in an operational servo system.

The sensitivity of such a measure to focus is seen to be activity dependent; i.e., the ac power of a sector does not perform well as a focus measure when the maximum activity of the sector, regardless of focus, is low. This result of not focusing well on low activity image areas agrees with the manner in which an operator would focus an image. Rather than examining, say, the sky or a dim background while adjusting the lens, he would look at the same sharp edge or fine texture to determine focus. In both the human and automatic cases, sufficient ac high-frequency energy must be locally present to evaluate an image's state of focus.

If, in the case of automated focusing, each subarea of the image in question cannot be examined in a reasonable time, then a criterion of minimal activity would have to be established. Only those subareas satisfying such a criterion would then be considered as useful input data to the focus evaluating device.

The division of activity information into texture and edge appears to be of little use in evaluating the state of focus of an image. The behavior of both texture and edge activity as well as those of the other image descriptors will continue to be evaluated in subsequent experiments.

2.5 CONCLUSIONS

The local ac power, or activity, of an image demonstrates each of the five characteristics desired of a focus measure presented in paragraph 2.1. It can be computed in a time span that is compatible with a real time system; its sensitivity

to focus can rival that of an observer: it has a good signal-to-noise ratio; it exhibits scene independence, subject to the limitations set forth a priori; and, since it is a simple scalor value that may be computed for each image frame, it is easily adaptable to an operational system. A real time imaging system that has an auto focus capability is certainly feasible and easily implementable using the two dimensional sensor processor.

SECTION 3

AUTO DEBLUR

3.1 INTRODUCTION

Automatic image deblurring seeks a means for characterizing the blur process, inverting it, and deriving a measure of the residual error. Blur characterization uses physical principles to narrow the anticipated range of possibilities, and then applies blind deconvolution to arrive at a specific form. Blur inversion undoes the degradation up to the point that ambient noise will allow. Error measurement uses either a mean square error (MSE) criterion or the set of image descriptors, each with its own particular merits.

Blur characterization therefore represents a preliminary step, followed by error measurement. Results from these steps set the ground rules and, to a certain extent, provide insight in addressing the inversion problem. Primary attention here will be devoted to the first two steps.

3.2 SPECIFIC BLUR TYPES

Blurs that afflict FLIR systems divide into several types:*

a. Aperture $\sim J_1 \, (kr)/kr \sim \bar{e}^{(r/r_o)^2}$

b. Scan $\sim \text{rect}\left(\dfrac{x}{\Delta x}\right) \text{rect}\left(\dfrac{y}{\Delta y}\right)$

c. Atmospheric $\sim \pi\left(\dfrac{r}{r_o}\right) \sim \bar{e}^{(r/r_o)^2}$

Each type characterizes the limited spatial frequency passband of an element in the chain of transfer functions that relate the original object (input) to the final

---

*Additional types include depth-of-focus and image-motion blurs. These will be treated as time permits. Depth of focus will probably receive priority; many others are currently investigating image motion effects.

image (output). Together, they play a role somewhat analogous to the well-known transfer function.

Aperture type blurring arises from the failure of limited-sized optics to capture a sufficient portion of the object's spatial frequency spectrum. The correspondingly limited bandwidth B does not permit resolution element sizes smaller than 1/2B, using classical imaging techniques. This result derives from Nyquist's Sampling Theorem and agrees substantially with the well-known Rayleigh criterion.

Physically, B varies directly with aperture size D, but inversely with object-aperture separation z. Consider a one-dimensional analog. At any given wavelength λ, the object's radiating field strength $g(x)$ will transform to

$$\int_{-\infty}^{\infty} g(\acute{x}) \, e^{i\pi(x-\acute{x})^2/\lambda z} \, d\acute{x} \sim G\left(\frac{x}{\lambda z}\right) \tag{1}$$

$$G(\cdots) = \text{Fourier transform of } g(\cdots)$$

upon reaching the aperture plane.*

An aperture that admits light only between $x = \pm D/2$ alters this to read

$$G\left(\frac{x}{\lambda z}\right) \text{rect} \frac{x}{D} \tag{2}$$

$$\text{rect} \frac{x}{D} = \begin{cases} 1, & \text{for } |x| < D/2 \\ 0, & \text{otherwise} \end{cases}$$

Subsequent optics generally seek to reverse the process that changed g into G. This, however, amounts to inverse Fourier transformation of the above expression, i.e.,

---

*Proof of this relation follows from expanding the quadratic exponent and observing that all terms other than the cross product can be disregarded, to a first approximation. Relatively small objects yield non-zero $g(x)$ only over a small interval about $x = 0$. At large values of z, this effectively suppresses the quadratic exponential term in x^2. Likewise, small apertures permit elimination of x^2. Integration of $g(x)$ with the exponentiated crossproduct yields the above transform relation.

$$g(\hat{x}) * \frac{\sin 2\pi B\hat{x}}{2\pi B\hat{x}} \sim \left\{ \begin{matrix} \text{Field Strength of} \\ \text{Reconstructed Image} \end{matrix} \right\} \tag{3}$$

$$|g(\hat{x})|^2_* \left(\frac{\sin 2\pi B\hat{x}}{2\pi B\hat{x}} \right)^2 \sim \left\{ \begin{matrix} \text{Intensity of} \\ \text{Reconstructed Image} \end{matrix} \right\}$$

$$B = \frac{D}{2\lambda z}$$

One-dimensional aperture-type degradation, therefore, corresponds to a blur function of the form $[\sin(\cdots)/(\cdots)]^2$. In two dimensions, the analogous aperture would be a circular hole of diameter D. A similar derivation would yield blur function

$$\left[\frac{J_1(2\pi Br)}{2\pi Br} \right]^2 \tag{4}$$

$$\gamma = \sqrt{x^2 + y^2}$$

$$J_1 = \text{first order Bessel function}$$

Scan-type blur characterizes the limited resolution resulting from sampling the output of the FLIR scanning mechanism. This image acquisition format will most likely be encountered in the second generation FLIR. Horizontal resolution distance can be expressed as

$$\Delta x = \frac{v}{2B}$$

$$v = \text{Horizontal scan velocity} \tag{5}$$

$$B = \text{Photoelectronic bandwidth} = [2(\text{Sample time})]^{-1}$$

while vertical resolution distance Δy is fixed by the distance between scan lines. These considerations dictate the blur function

$$\frac{\sin\left(\frac{2\pi Bx}{v}\right)}{\frac{2\pi Bx}{v}} \text{rect}\left(\frac{y}{\Delta y}\right) \tag{6}$$

A symmetrizing approximation

$$\text{rect}\left(\frac{2\pi Bx}{v}\right)\text{rect}\left(\frac{y}{\Delta_y}\right) \tag{7}$$

however may be preferred.

Atmospheric blur arises from scattering phenomena, such as haze, and from clear air turbulence. Scattering generally attenuates all radiation wavelengths smaller than a given cutoff limit. It therefore dictates an upper limit on B in equations (3) and (4).

Clear air turbulence produces blurring by creating random spatial and temporal density variations. The resulting spurious diffraction tends to warp incident wavefronts and, generally, to degrade mutual coherence. Mutual coherence expresses the degree to which neighboring points on a reference plane across incident radiation designate fixed (if unknown) phase relations with respect to one another. Drawing a so-called coherence circle about a chosen point P in this plane, the phases associated with all interior points are more or less correlated with P, while exterior point phases exhibit little or no P-correlation.

Coherence circle diameter decreases with range.* This diameter sets a practical upper limit on the desired aperture size. Larger apertures increase image intensity, but not resolution. As in scattering, therefore, turbulence introduces no new types of blur function. Rather, it restricts parameters in the $[J_1 (\cdots)/(\cdots)]^2$ form associated with aperture-limited blur.

3.3 BLUR SIMULATION

Aperture-type blurs can be simulated by pinhole masks or by computer. A pinhole mask of radius r_o will impose a blur of the form in (4) with $B = r_o/\lambda f$ when introduced, as in Figure 3-1.

_____

*According to V. I. Tataiski's "Wave Propagation in a Turbulent Medium," the diameter shrinks as the -3/5 power of the range. Quantitative aspects of his theory have been disputed by later authors, but the general shape of the decreasing trend seems to be accepted.
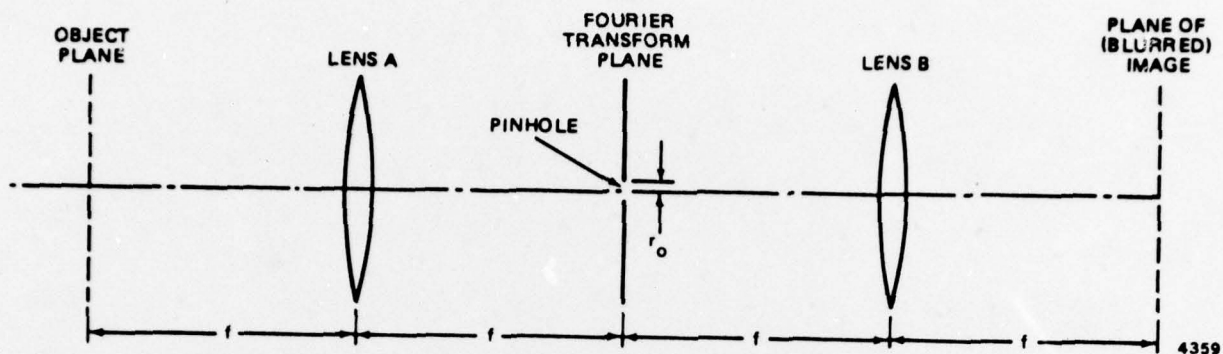
Figure 3-1.   ANALOG SCHEME FOR INTRODUCING APERTURE-TYPE BLURS

Computer implementation would approximate (4) by

$$\frac{1}{4} \ e^{-\left(\frac{\pi B r}{2}\right)^2} \tag{8}$$

and then sample it uniformly over x and y according to the rule

$$x^2 + y^2 = m^2 \ (\Delta x)^2 + n^2 \ (\Delta y)^2 \le r_{max}^2 \tag{9}$$

   m,n = integers

$\Delta x = \Delta y$ = linear pel size

$r_{max} \sim 4/\pi B$

The procedure simplifies the form and spread of the blur function, and reduces the result to a discrete set of pel values. This, in turn, permits discrete convolution of original image with blur function in a format suited to the computer.

3.4 EXPERIMENTAL PROCEDURE

These considerations form the basis of a quantitative experimental approach to blur simulation, measurement, and removal. Nominal goals include:

- Quantitative characterization of naturally occurring blurs
- Determination of practical limits on deblur improvements
- Understanding the impact of real-time constraints.

Towards these ends, the experimental procedure will follow along the lines of Figure 3-2.

Transparencies will be chosen to emphasize four major types of features: (1) fine linear details with horizontal and vertical orientations, (2) fine linear details with diagonal orientation, (3) details giving rise to concentric-circular patterns, and (4) finely resolved scenes with no preferred orientation. This will include at least one chart whose individual test patterns emphasize (1) through (4). Current plans call for computer implementation of blur simulation on a few initial sample scenes, during construction of the analog lens scheme. The analog scheme can then be used for rapid appraisal of a larger number of scenes.
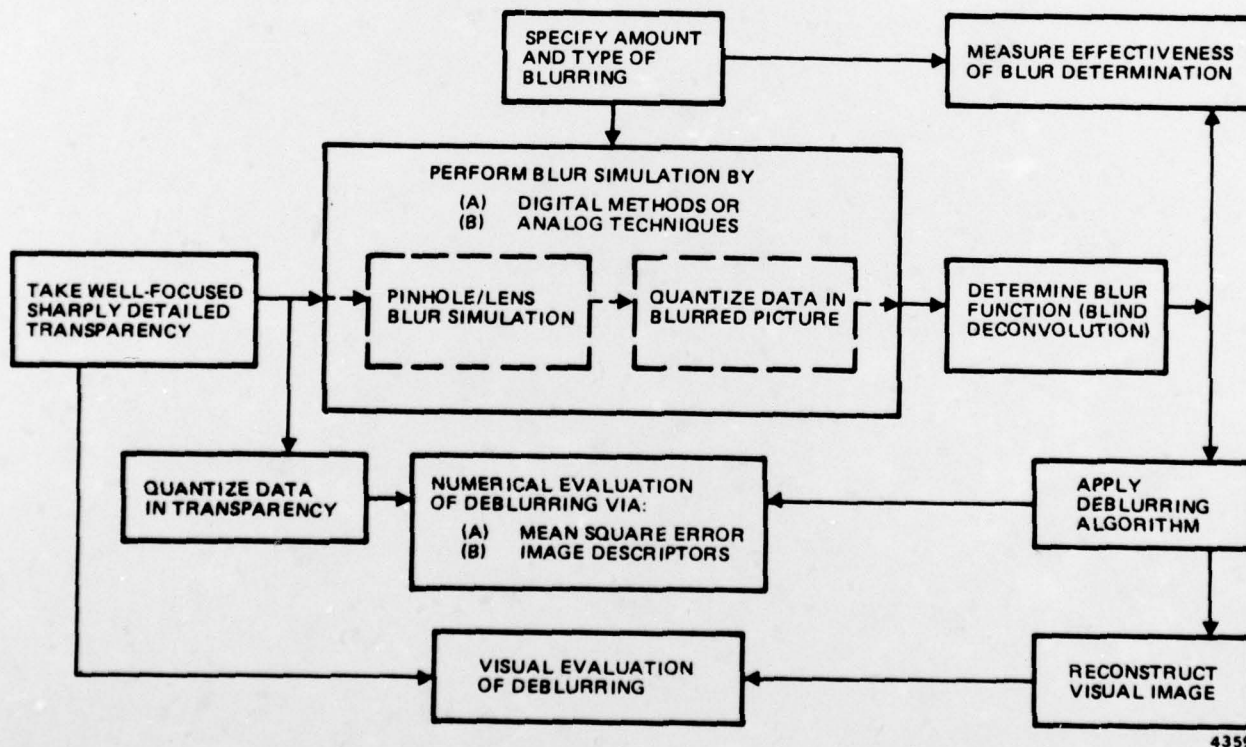

Figure 3-2. GENERAL EXPERIMENTAL PLAN FOR AUTO DEBLUR

Each transparency corresponds to about 120 pels per inch, i.e., a resolution distance of 0.02 cm. Combined with a focal distance of 10 cm and a nominal wavelength of 0.3 μm, this yields a maximum pinhole diameter of 150 μm. Controlled blurring is achieved by cutting the actual pinhole size to fractions of this maximum value (see Table 3-1). Pinholes of these sizes are readily available and relatively inexpensive.

Table 3-1. PINHOLE SELECTION

Pinhole Diameter (μm)	Fraction of D_{max}	Resolution Length in cm	Resolution Length in Pels
10	1/15	0.3176	15
25	1/6	0.1270	6
50	1/3	0.0635	3
100	2/3	0.0375	1.5
150	1	0.0200	1

Blur function determination represents a key phase of the experimental program. Three alternative approaches will be investigated. These include an empirical search for an all-purpose blur function, techniques that use the asymptotic behavior of the Haar coefficients, and techniques that attempt simplifying mathematical approximations.

The empirical alternative would examine the spatial frequency bandwidths of a large number of scenes that have all been subjected to the same specific blur simulation.* The maximum of these bandwidths will define a pill-box type blur function of diameter $1/2B_{max}$**. This result can be compared to the true value of B, which characterizes the simulation. The comparison may indicate near-equality, a fixed ratio, or some other significant relationship between the two quantities.

---

*If the intended use implies a characteristic type of terrain, visibility or other feature, the above scenes should all be chosen to include that feature.

**Some authors have designated the pillbox function as $\pi(\cdots)$; in this case, $\pi(2B_{max} r)$ where $r = \sqrt{x^2 + y^2}$.

The asymptotic approach would use the ability of the Haar expansion to generate local functions (higher order terms) as well as global ones (lower order). Because the local functions describe any restricted area of the scene, they open the possibility of superimposing the different areas in such a manner that scene information will decorrelate and wash out, while blur information will correlate and reinforce. This, in effect, could provide a Haar transform approach to the blind deconvolution techniques using the Fourier transform that were developed by Cole and Stockham at the University of Utah.

Using a one-dimensional analog for simplicity, coefficients $a(r,m)$ of Haar expansion

$$g(x) = \sum_r \sum_m a(r,m)h(r,m,x) \tag{10}$$

where: $h(r,m,x)$ = Haar function of sequency r and offset $m \cdot 2^{-r}$

can be grouped into subsets $a(r,1)$, $a(r,2)$, $a(r,3)$, ..., $a(r,k)$, ... In each subset, the magnitudes of the a's will drop off beyond some high sequency cutoff $r = r_k$. The average value and/or linear combinations of the r_k can then be compared with the resolution distance imposed by the simulated blur.

The third approach convolves the Haar expansions of unblurred figure $g_1(x)$ and blur function $b(x)$ to obtain an expression for blurred image $g_2(x)$:

$$g_2(x) = g_1(x)*b(x) = \sum_{(r,m)} \sum_{(p,k)} a(r,m)b(p,k)[h(r,m,x)*h(p,k,x)] \tag{11}$$

Function $h_k(x)$ can be regarded as a matched filter and $h_p(x)$ as the candidate waveform. Unless k and p refer to the same sequency, the convolution should produce zero to a first approximation. This in turn should yield

$$g_2(x) \doteq \sum_r \sum_{m=o}^{k} a(r,m)b(r,k) \, w[x - (m,k)2^{-r}, \, r] \tag{12}$$

where w is the symmetric W-shaped waveform resulting from the convolution of an r-sequency Haar function with itself. This form would be used to characterize subsections of the image, each with distinct sets of $a(r,m)$ but with a common set of $b(r,k)$. Some variation on the usual approach to blind deconvolution would then be

used to extract the b's. These results can be compared to the Haar coefficients of simulated blur actually imposed.

Deblurring algorithms will generally seek to retrieve higher order portions of the Haar spectrum, which have been suppressed by blurring. Initial experiments will evaluate the effect of high sequency amplification as a restorative process. For these, a noiseless or very low noise environment will be assumed. Further experiments will then account for realistic noise levels through a Haar transform approach to optimum filter theory.

This theory generally proposes direct blur inversion in regions where the signal-to-noise ratio (SNR) is high, but further deliberate blurring where the SNR is low. Different settings of the boundary between high and low will determine whether the result will show good deblurring at the cost of high noise or a more moderate tradeoff.

The experimental procedure will determine the Haar image spectrum and the general spectral level of the noise. The regions where the image rises above the noise can then be identified. A Haar implementation of inverse blurring will be applied to these regions, while further blurring will be applied to the alternate (low SNR) regions.

3.5 MEASUREMENT OF RESULTS

Quantitative assessment of the blurring effect can use either mean square error (MSE) or image descriptor (ID) criteria. In MSE, a pel-by-pel subtraction between original and blurred images is followed by squaring and summing. This numerical result will generally increase with progressive blurring. An intuitive proof would compare the original image, with its relatively dense forest of sampled values, against a thinned version corresponding to the blurred result. With greater blurring, even more sample values would be deleted. If N represents the number of deleted values at any stage of blurring, then a simple statistical argument shows that

$$(MSE) \sim \frac{N}{A} \overline{g_n^2} = \frac{N_o}{A} \frac{\Delta B}{B_o} \overline{g_n^2} \tag{13}$$

3-9

where:

g_n = intensity of $n\underline{th}$ pel in original image

A = Area of projected image

B_o, N_o = Original bandwidth and number of samples

ΔB = Bandwidth reduction causing blur

In terms of ID's, the expression for MSE can be interpreted as the activity per unit area. Thus,

$$\frac{(Activity)}{N_o g_n^2} = \frac{\Delta B}{B_o} = \begin{Bmatrix} \text{Relative} \\ \text{Resolution} \\ \text{Degradation} \end{Bmatrix} \tag{14}$$

3.6 FUTURE EFFORTS

Follow-on goals include real-time algorithms that derive the particular blur via blind deconvolution, enhancing the efficiency of these algorithms by restricting their search to $J_1 (\cdots)/(\cdots)$ and rectangular blur types, and using these results to derive a real time deblurring process. Haar processing will be used to the extent that it simplifies these tasks.

Blind deconvolution essentially multiplies spectra of different portions of the image and then takes the $k\underline{th}$ root where k = number of portions. The division of the image into 16 by 16 pel blocks in the current 2D Haar processor will facilitate this goal. A further advantage will arise from the deterministic nature of the rectangular blur. In the final deblurring process, tradeoffs between simplicity and the sacrifice of real time for near-real time operation will be studied.